Characterization of atmospheric water-soluble brown carbon in the Athabasca Oil Sands Region, Canada.

Dane Blanchard[1], Mark Gordon[2], Duc H. Dang[1,3], Paul A. Makar[4], Julian Aherne[1]

[1]School of the Environment, Trent University, Peterborough, Ontario, Canada K9J 7B8
[2]Earth and Space Science, York University, Toronto, Canada M3J 1P3
[3]Department of Chemistry, Trent University, Peterborough, Ontario, Canada K9J 7B8
[4]Air Quality Research Division, Environment and Climate Change Canada, Toronto and Montreal, Canada

Correspondence to: Dane Blanchard (daneblanchard@trentu.ca)

Abstract. Extensive industrial operations in the Athabasca Oil Sands Region (AOSR), Alberta, Canada, are a suspected source of water-soluble brown carbon (WS-BrC), a class of light-absorbing organic aerosols capable of altering atmospheric solar radiation budgets. However, the current understanding of WS-BrC throughout the AOSR is limited, and the primary regional sources of these aerosols are unknown. During the summer of 2021, active filter-pack samplers were deployed at five sites throughout the AOSR to collect total suspended particulate for the purpose of evaluating WS-BrC. Ultraviolet – visible spectroscopy and fluorescence excitation-emission matrix (EEM) spectroscopy, complimented by Parallel Factor Analysis (PARAFAC) modelling, were employed for sample characterization. Aerosol absorbance was similar between near-industry and remote field sites, which suggested industrial WS-BrC exerted limited influence over regional radiative forcing. Combined EEM-PARAFAC analysis identified three fluorescent components (fluorophores), including one humic-like (C1) and two protein-like (C2, C3) substances. Sites near oil sands facilities and sample exposures receiving atmospheric transport from local industry (indicated via back-trajectory analysis) displayed increased C1 and C3 fluorescence; moreover, both fluorophores were positively correlated with particulate elements (i.e., vanadium, sulphur) and gaseous pollutants (i.e., nitrogen dioxide, total reduced sulphur) indicative of oil sands emissions. Fluorophore C2 presented high emission intensity at near-field sites and during severe wildfire smoke events, while positive correlations with industry indicator variables suggested C2 was likely reflective of both wildfire-generated and anthropogenic WS-BrC. These results demonstrated that combined EEM-PARAFAC analysis is an accessible and cost-effective tool that can be applied to monitor industrial WS-BrC in the ASOR.

1 Introduction

Water-soluble brown carbon (WS-BrC) represents a class of organic aerosols capable of absorbing light within the ultraviolet (UV) and visible (Vis) wavelength ranges (Basnet et al., 2024; Lin et al., 2012; Stone et al., 2009). Chemical species within the WS-BrC fraction are classified as chromophoric dissolved organic matter (CDOM), which generally consists of polymerized, aromatic, humic-like substances (HULIS) and lower molecular-weight protein-like substances (PRLIS). Both HULIS and PRLIS represent broad chemical groups named according to their chemical and optical similarity to humic matter and proteins found in terrestrial, aquatic, and atmospheric environments (Dey and Sarkar, 2024; Duarte et al., 2007; Laskin et al., 2015).

Owing to their light-absorbing properties and capacity as cloud condensation nuclei (CCN), WS-BrC particles can influence planetary albedo and solar radiation budgets (Zhou et al., 2023; Liu et al., 2015), and as such have been recognized as an influential factor in climate change research (Chakrabarty et al., 2016; Gustafsson et al., 2009). Moreover, soluble BrC has been found to play an important role in atmospheric reaction chemistry (Jiang et al., 2012) and can be detrimental to human health (Li et al., 2017;

Ma et al., 2019). Biomass and fossil fuel combustion are the dominant sources of atmospheric WS-BrC, including HULIS and PRLIS (Claeys et al., 2012; Wu et al, 2019; Zeng et al., 2022); however, biogenic emissions, soil dust, and industry can all contribute to primary and secondary formation of these organic aerosols (Spranger et al., 2020; Wu et al., 2019).

Industrial operations in the Athabasca Oil Sands Region (AOSR) in north-eastern Alberta, Canada, are a substantial source of atmospheric particulate matter (PM) (Giesy et al., 2010; Landis et al., 2017; Liggio et al., 2016). Open pit mining activities, haul road dust, dry tailings, vehicle exhaust, and upgrading facilities are sources of organic–containing PM (Giesy et al., 2010; Zhang et al., 2016), while volatile precursor emissions from flue gas stacks and exposed bitumen contribute to secondary organic aerosol formation (Liggio et al., 2016). Organic PM generated from oil sands (OS) activities consists of a diverse range of chemical species, including polycyclic aromatic compounds (PAC: Bari and Kindzierski, 2018; Liggio et al., 2016; Liggio et al., 2017), oxygenated polycyclic aromatic hydrocarbons (Jariyasopit et al., 2021), naphthenic acids (Yassine and Dabek-Zlotorzynska, 2017), and organic matter linked to surface-soil and overburden dust (Wang et al., 2015). An unresolved fraction of these emissions contains relatively water-soluble species (Arp et al., 2014; Josefsson et al., 2015; Marentette et al., 2015), which can contribute to the WS-BrC fraction, partially due to their conjugated structures (Stedmon and Nelson, 2015).

Relatively little was known regarding the abundance and composition of WS-BrC in the AOSR airshed, nor was it well understood how local industry contributed to the CDOM fraction. Considering the magnitude of sources in the region, OS emissions likely contributed to WS-BrC, which in turn could influence radiative forcing on a broad scale. The established toxicity and environmental mobility of water-soluble organic pollutants (Lemieux et al., 2008; Lundstedt et al., 2007) provide a clear incentive to monitor these species throughout the AOSR; however, the diversity of WS-BrC chemical formulae presented a challenge to regional monitoring efforts, due to the high operational costs of typical mass spectrometry methods (Frysinger et al., 2003).

Ultraviolet-visible (UV-vis) spectroscopy is commonly employed to characterize the bulk properties of environmental CDOM. Moreover, a sizable fraction of WS-BrC consists of fluorescent dissolved organic matter (Laskin et al., 2015) which can be evaluated through the application of excitation emission matrix (EEM) spectroscopy. Complex EEM datasets can undergo processing via Parallel Factor Analysis (PARAFAC); a multivariable model that can identify fluorescent components (fluorophores) reflective of organic compounds with shared optical properties. Fluorescence EEM spectroscopy and PARAFAC modelling has been successfully used to identify WS-BrC originating from a variety of biogenic and anthropogenic sources (Harsha et al., 2023; Wu et al., 2019; Zito et al., 2019).

In this study we evaluated WS-BrC quality in the AOSR and assessed the influence of OS activities over the organic PM fraction through the application of UV-vis and fluorescence spectroscopy techniques. During the Summer of 2021 (July 19–August 10), active filter-pack samplers were deployed at five sites throughout the study region to collect atmospheric PM for optical and chemical analysis. Fluorescent analysis of local reference materials and back-trajectory modeling were used to assist with source identification, while partial least squares regression (PLS-R) analysis was employed to characterize individual fluorophores generated by the PARAFAC model.

2 Methods

2.1 Study area and sampling sites

The AOSR is situated within a Boreal Plains ecozone, where peatlands and boreal forests are the dominant landscape features. Largely because of its northern inland geographical location, the region typically experiences warm summers and cold dry winters

(ECCC, 2024). Beneath the boreal landscape lies the Athabasca oil sands deposit, the world's largest known bitumen reserve, which covers a surface area of ~ 140 200 km^2. Oil and gas companies such as Syncrude, Suncor, and Imperial Oil have established industrial facilities over these deposits to extract bitumen and upgrade it to refined material such as crude oil. The major OS facilities are located along the east and western banks of the Athabasca River (which flows North through the AOSR), as the Athabasca bitumen layer is close to the surface in these areas. The largest municipalities in the region are Fort McMurray and Fort McKay; the former is located ~50 km south of major OS operations while Fort McKay sits along the western bank of the Athabasca River, situated between several major industrial facilities (Figure 1).

The Wood Buffalo Environmental Association (WBEA; https://wbea.org) operates an extensive network of continuous air-quality monitoring stations and atmospheric deposition monitoring plots throughout the AOSR. Between July 19th to August 10th, 2021, active filter-pack systems for this study were co-deployed at five WBEA sites located throughout the AOSR to collect back-to-back 48 h exposures. Two of these fence-line sites (Mildred Lake deposition plot [DP2050]; Bertha Ganter station [AMS01]) were located in close proximity (DP2050 < 1 km, AMS01 < 5 km) to OS facilities (consisting of tailings ponds, open pit mines, haul roads, upgrading facilities), a second set of stations (Patricia McInnes [AMS06]; Athabasca Valley [AMS07]) were situated in suburban/community locations > 50 km south of major OS operations, while a final background station (Stoney Mountain [AMS18]) was located ~ 150 km south of OS operations (Figure 1). Differences in observations between the stations thus allowed us to infer sources associated with OS versus other activity. The selected WBEA stations continuously monitored a variety of air quality and meteorological data, including sulphur dioxide (SO_2), total reduced sulphur (TRS), nitrogen oxide (NO), nitrogen dioxide (NO_2), total hydrocarbons (THC), carbon monoxide (CO), fine particulate matter ($PM_{2.5}$), wind speed, wind direction, temperature, and relative humidity.

During the year of 2021, 4.30 x 10^6 hectares of land across Canada were burned by wildfire compared to the 2013–2022 ten-year annual average of 2.73 x 10^6 hectares (source: Canadian Interagency Forest Fire Center Inc.). As a result of increased fire magnitude, substantial portions of western Canada were periodically blanketed in smoke plumes during the study period. Wildfire emissions are a substantial source of atmospheric PM and BrC (Chen and Bond, 2010; Guan et al., 2020), which can contain aromatic pollutant species with fluorescent properties (Veselovskii et al., 2020). To account for the potential influence of wildfire emissions over observed fluorescence, the temporal variability of $PM_{2.5}$ was assessed at each WBEA monitoring station to identify sampling periods of high fire smoke transport.

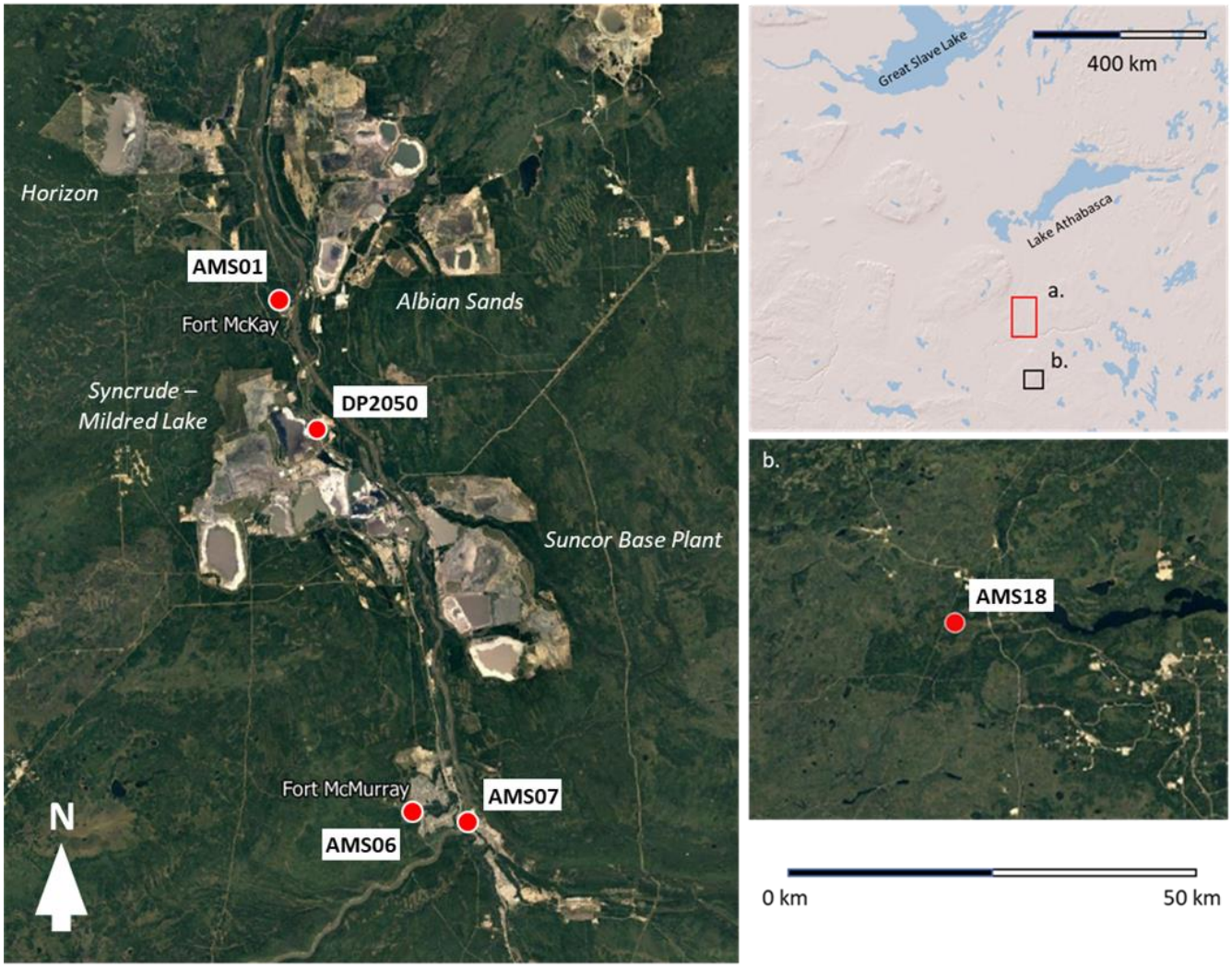

Figure 1: Distribution of active sampler sites (red circles) throughout near/mid-field (a) and far-field (b) study regions. Nearby communities (Fort McMurray, Fort McKay) and major active oil sands facilities are shown (© Google Maps 2024). The map on the top-right displays the location of the two regions on a broader spatial scale (© ESRI 1995-2024).

2.2 Active sampling

Active samplers consisted of a 15 liter per minute (L min^{-1}) vacuum pump connected to an in-line flowmeter and filter-pack cartridge inlet. These systems were directly powered through an AC outlet available at the WBEA monitoring stations, while a 12 V marine battery served as the power supply for a 7.5 L min^{-1} vacuum pump at the off-grid DP2050 deposition plot.

The filter-pack cartridges used in this study were obtained through the Norwegian Institute for Air Research (NILU; www.nilu.no) and consisted of two threaded compartments that housed pre-combusted quartz fiber filter (47 mm diameter, 0.3 µm aerosol retention) intended to collect total suspended particulate (TSP). After each exposure, filters were placed in a petri-dish, triple sealed in Ziploc® plastic bags and stored at – 20 °C until analysis. In total, 44 filter-pack samplers were successfully deployed (48 h exposures) during the field campaign, which broken-down by site included: 11 at AMS01 and Mildred Lake, 10 at AMS06, 8 at AMS18 and 4 at AMS07, respectively (Figure S1). During the study period, five of the forty-four samples were collected as duplicates through the deployment of two sampling units. Five additional quartz fiber filters were allocated as field blanks during the study period and were stored like exposed filters.

Prior to the field survey all components of the filter-pack cartridge were individually rinsed in reverse osmosis water and subsequently soaked in a 2 M hydrochloric acid (HCl) bath for 12 hours, after which the sampler parts were rinsed in ultrapure lab water (Milli-Q). In the field, the filter-pack cartridges were soaked in baths of Milli-Q water between exposures. To control for potential filter contamination between exposures, field blanks were loaded into (as if to collect a sample) and subsequently removed from select washed cartridges.

Following exposure, a 20 mm diameter sub-section of the filter was removed via circular punch, and subsequently extracted in conical vials containing 50 ml of Milli-Q water. Sample vials were inverted three times, placed in an ultrasonic bath for 1 hour, and filtered (nylon; 0.45 µm). Filtered samples were stored at ~ 4 °C and underwent optical analysis within 12 hours of initial extraction. A 0.5 ml aliquot was used for determination of anionic species (Cl^-, NO_3^-, SO_4^{2-}) via ion chromatography (Dionex ICS-1100) while a separate 10 ml aliquot was acidified (2% HNO_3) and sent to the Water Quality Center at Trent University (Peterborough, Ontario, Canada) for determination of dissolved elements (Na, Mg, P, S, K, Ca, V, Cr, Mn, Fe, Zn, Sr) using an Agilent 8800 triple quadrupole inductively coupled plasma mass spectrometer. Additional details regarding instrument configuration and measurement parameters are available in the appendix section A1. A filtered 20 ml aliquot was used for determination of water-soluble organic carbon (WSOC), dissolved inorganic carbon (DIC), and total dissolved nitrogen (TDN) via Shimadzu TOC-V analyzer. The remaining filtered solution was adjusted to pH ~ 6.5 using 0.1 M sodium hydroxide (NaOH) or HCl to limit the influence of variable sample pH over WS-BrC optical properties (Lakowicz, 2006). Blank samples were used to determine method detection limits (MDL), which were calculated as: standard deviation (blank samples) × t-value 99.0% confidence critical value (3.747).

Measured analytes from the filter extracts were converted to time-integrated atmospheric concentrations using the following equation:

$$C = \frac{(C_e - C_b) * V_e}{V_a} * A_f * 1000 \quad (1)$$

Where C is the atmospheric concentration (ng m^{-3}), C_e is the analyte concentration (µg L^{-1}) within the filter extraction solution, C_b is the analyte concentration within the field blank extraction solution, V_e is the extraction solution volume (L), V_a is the volume of air sampled (m^{-3}), and A_f is the surface-area ratio (5.52) to account for the 20 mm filter cut-out.

2.3 UV-Vis spectroscopy

Absorbance was measured along a range of wavelengths (λ) between 200 to 800 nm (1 nm intervals) using a Cary 100 UV-vis spectrophotometer from Agilent Technologies. Filter extracts were allowed to warm to room temperature (~ 21 °C), and subsequently placed in a 1 cm (3.5 ml) Hellma® Suprasil® quartz cuvette (Hellma 101-QS) for analysis. A blank sample of Milli-Q water was first used to establish an instrument baseline. To clean, cuvettes were soaked in a 2 M HCl bath for ten minutes followed by subsequent rinses in Milli-Q water, 95% ethyl alcohol, and a final rinse in Milli-Q. The aerosol light absorption coefficient (Abs_λ, m^{-1}) at wavelength λ was calculated by the equation (Wu et al., 2019):

$$Abs_\lambda = (a_\lambda - a_{700}) \times \frac{V_w}{V \times l} \times \ln(10) \quad (2)$$

Where V_w refers to the volume (ml) of the filter extraction, V is the volume of air sampled (m^3) during the field exposure, l is the optical path length (cm), while a_λ and a_{700} are the absorbance at wavelengths λ and 700 nm, respectively. Absorbance at 700 nm is used as a reference to account for baseline drift. The light absorption coefficient at 365 nm (Abs_{365}) is frequently referenced as a

proxy for BrC in the literature (Laskin et al., 2015; Wu et al., 2019), and is subsequently used to calculate the mass absorption efficiency (MAE_{365}, m^2 g C^{-1}) via the following equation (Wu et al., 2019):

$$MAE_{365} = \frac{Abs_{365}}{C_a} \quad (3)$$

Where C_a is the atmospheric concentration of WSOC (µg C m^{-3}), obtained using Eq. 1. Both Abs_{365} and MAE_{365} are frequently used in the literature to assess the radiative forcing potential of BrC aerosols (Dong et al., 2024; Yue et al., 2019).

2.4 Fluorescence spectroscopy and PARAFAC

Combined EEM and PARAFAC analysis is commonly used to evaluate the optical and structural characteristics of environmental CDOM since the modelling technique can identify the excitation and emission peaks of multiple distinct fluorophores (i.e., HULIS, PRLIS) within EEM scans (Harsha et al., 2023; Wu et al., 2019). Fluorescence analyses was conducted using a Cary Eclipse spectrophotometer set to the three-dimensional EEM scan and signal to reference (S/R) acquisition modes. Sample aliquots were placed in a 1 cm (3.5 ml) quartz cuvette (Hellma 101-QS) for analysis. Excitation (λ_{Ex}) and emission (λ_{Em}) scans (both measured at 5 nm intervals) ranged from 200–450 nm and 250–600 nm, respectively. A Milli-Q water blank was first measured to zero the fluorometer, then subsequent blanks were scanned every five samples. During each day of analysis, a set of quinine sulphate standards were prepared to create a calibration curve (1–100 ppb quinine sulphate in 0.5 M sulphuric acid) to convert fluorescence intensity measurements into quinine sulphate units (QSU) (Sui et al., 2017). To minimize the potential influence of the inner filter effect (IFE) over the fluorescence spectrum, all filter extracts were confirmed to have an absorbance < 0.05 at 270 nm (Trubetskoj et al., 2018).

Fluorescence data was processed via the R package "staRdom", which was used for blank and spectrum correction (Pucher et al., 2019). Inner filter effect corrections were applied to individual EEMs using the built-in IFE function and corresponding sample absorbance values (Shimadzu spectrophotometer). Rayleigh and Raman light scattering bands were removed from each sample EEM, and the empty cells infilled using the "eem_interp" function. The fluorescence intensity data was then divided by the corresponding extraction solution and air volume to convert QSU to QSU per cubic meter (QSU m^{-3}) (Deng et al., 2022). The EEM dataset displayed limited fluorescence within the 540–600 emission and 400–450 excitation wavelength ranges, thus these regions were removed prior to PARAFAC modeling. Using the staRdom package, a PARAFAC model was employed to decompose the three-dimensional EEM data array (X_{ijk}) into a score matrix (A) and two loadings' matrices (B and C) with corresponding tri-linear elements a_{if}, b_{jf}, *and* c_{kf} (Bro 1997):

$$x_{ijk} = \sum_{f=1}^{F} a_{if} b_{jf} c_{kf} + e_{ijk} \quad (4)$$

Score values in a_{if} represent the relative fluorescence intensity of fluorophore *f* in sample *i*, the elements b_{jf} and c_{kf} represent the modelled emission (*j*) and excitation (*k*) loadings (i.e., wavelength coordinates) of *f*, while *F* is the total number of modelled fluorophores. Utilizing the residual element e_{ijk}, the PARAFAC model applies an alternating least-squares optimization technique to find the function that best approximates the dataset (Bro, 1997).

The appropriate number of modelled components (model rank) was selected based on four validation tools, including: 1) visual peak inspection, 2) EEM residual plots, 3) split-half analysis, and 4) core consistency (CC). Visual inspection provides an initial check to confirm the modelled components present well-defined emission peaks, which suggests that the spectra represent a distinct fluorophore or a group of similarly fluorescing species. The model residuals corresponding to each sample (e_{ijk}) can be plotted as a function of λ_{Ex} and λ_{Em}. These plots can be visually inspected to identify potential peaks, where a high abundance of such features

across the dataset would indicate that the model rank is not representative of the array (Driskill et al., 2018; Murphy et al., 2014). Split-half analysis involved division of the EEM dataset into a set of four equal-sized groups, where independent PARAFAC models were generated for each subgroup and subsequently compared to measure similarity via Tucker Congruence Coefficient (TCC; Pucher et al., 2019). A high TCC similarity score (~1) signaled that the model was representative of the true variation within the fluorescence dataset. The model rank with the highest TCC score was most likely the appropriate selection (Bro, 1997; Stedmon et al., 2003). Core consistency is a measure of the regression between the three-way array of the PARAFAC model and the core array of a Tucker3 model generated from the corresponding EEM data. A CC score between 90% to 100% indicated a strong model, while values ≤ 50% suggested a problematic output. Generally, the largest model rank prior to a dramatic decline in CC should be selected (Bro and Kiers, 2003).

The sample score values assigned to individual fluorescent components (a_{if}) were reported according to maximum fluorescence (F_{MAX}, QSU m^{-3}). To account for the potential influence of bulk DOM fluorescence over individual fluorophore emission intensity (due to variations in DOM concentration between samples), modelled component F_{MAX} values were divided by sample WSOC concentration (µg C m^{-3}) to normalize component fluorescence.

2.5 Environmental reference materials

A variety of environmental reference materials representative of dominant TSP emission sources from the OS were collected for EEM analysis, including a) dust from an unpaved road near observation site AMS01 (composite grab-sample), b) dust from a heavily trafficked unpaved road near observation site DP2050 (composite grab-sample), c) raw bitumen ore from the Athabasca Deposit and, d) dry mature fine tailings from the AOSR (MFT; composite industrial sample; Innotech Alberta). Dry road dust and MFT were sieved to < 2 mm to remove coarse material (Lanzerstorfer and Logiewa, 2019), while raw bitumen was too viscous to sieve. Each reference material was extracted in Milli-Q water and diluted to achieve a WSOC concentration of ~ 1.0 mg C L^{-1} and an absorbance < 0.05 at 270 nm (to match the filter extracts). Sample extracts were adjusted to a pH ~ 6.5 using 0.1 M NaOH or HCl (to match the pH of BrC extracts) and then stored at ~ 4 °C prior to optical analysis.

2.6 Data analysis

Variability in sampler observations was assessed by calculating the relative percent difference (RPD, %) from duplicate filter-pack exposures. Data displayed a non-normal distribution as determined via Shapiro-Wilk test ($\alpha < 0.05$); thus, non-parametric statistical tests were employed for subsequent analysis. Median values were used as a measure of central tendency, while data variability was evaluated using normalized median absolute deviation. Bivariate associations between measured TSP analytes and continuous pollutants were evaluated via Spearman's Rank Order correlation test, and the Kruskal-Wallis test was used to determine significant differences between sampling locations.

Partial least squares regression (PLS-R) analysis was applied to assist with fluorescent component characterization (Kothawala et al. 2014). Partial least squares analysis is a multivariable regression technique that is effective at decomposing large numbers of colinear predictor variables (X) into a smaller set of uncorrelated orthogonal components (Eriksson et al., 2013). The PLS-R model attempts to explain the maximum variability between X and response variables (Y) through a least-squares regression method. Modelled fluorescent component values (QSU m^{-3}) were assigned as Y variables while additional elements, WSOC, DIC, and TDN were designated as X. The appropriate number of components was determined via internal cross-validation, where a random subset of samples (~ 10% of dataset) was removed from the training dataset to evaluate the model. The resulting comparisons were evaluated based on model rank cumulative goodness of fit (explained variation; R^2Y) and cumulative goodness of prediction (Q^2Y).

The relative influence of X variables over each component was interpreted via variable influence on projection scores (VIP), where values ≥ 1 signified a highly influential predictor variable (Eriksson et al., 2013). The spatial proximity of variable loadings served as a visual indicator of X and Y variable associations, while variable distance from the origin indicated the level of correlation with each component.

2.7 Trajectory analysis

The atmospheric transport model, HYSPLIT (Stein et al., 2015), was applied to evaluate source-receptor relationships within the study region. Meteorological data available through the Global Data Assimilation System was employed to generate bihourly backward wind trajectories (arrival height 10 m above ground level) spanning the duration (~48 h) of active sampler exposures at individual sites (i.e., 24 back-trajectories per exposure). The resulting trajectory data were overlain onto OS facilities (polygons representing tailings, open mine pit, plant site boundaries) to explore the influence of industrial sources over observed TSP fluorescence. Using these spatial data, the relative frequency (%) of back-trajectories intersecting OS-facility boundaries (T_{OS}) during each exposure was calculated to further explore source-receptor relationships. The frequency method counts the number of times air trajectories intersect individual grid points (0.5 × 0.5 degrees) in the model domain, and then normalizes that sum value by the total number of modelled trajectories (%). It should be noted that the trajectory estimates do not account for the influence of vertical mixing and lateral diffusion over pollutant transport.

Through the Canadian National Fire Database, spatial data representing the boundaries of Canadian wildfires active during the study period (July 19–August 10) were used to evaluate the potential influence of pyrogenic sources over observed fluorescence. Using the same Global Data Assimilation System meteorological datasets as before, additional HYSPLIT backward trajectory frequency plots were modelled to evaluate atmospheric transport patterns during multi-day wildfire smoke episodes.

3 Results

3.1 Meteorology and continuous pollutant summary

Limited variation in relative humidity occurred between monitoring stations during the study period, where median values ranged from 69.8% to 71.8% (Table 1). The AMS01, AMS06 and AMS07 stations experienced prominent winds blowing from a range of directions (excluding NE – E) during the study period, while S – W winds were dominant in AMS18. Wind speeds were higher at AMS06, while colder temperatures were recorded at AMS18. Moreover, the background station received a larger volume of precipitation compared with AMS01. Further, AMS01 experienced significantly higher CO, NO_2, SO_2, and TRS (Kruskal-Wallis; $\alpha < 0.05$) owing to its proximity to OS operations, while the lowest concentrations (with exception of CO) were recorded at the more distant downwind site AMS18 (Table 1). Ambient $PM_{2.5}$ was notably elevated at AMS18 with concentrations similar to AMS06 and AMS07.

Evaluation of WBEA station $PM_{2.5}$ timeseries data identified two periods of elevated concentrations. The first and most intense (hourly maximum $PM_{2.5} > 140$ µg m^{-3}) event occurred between July 19–22 while the second event ranged from July 31–August 6 (hourly maximum $PM_{2.5} \sim 50$ µg m^{-3}) (Figure S2). These high $PM_{2.5}$ events occurred during relatively similar periods between monitoring stations (including AMS18), suggesting a shared regional source. Trajectory frequency analysis indicated that extensive wildfires in northern Saskatchewan were the primary source of smoke ($PM_{2.5}$) in the study region (Figure S3).

The T_{OS} analysis demonstrated that the relative influence of OS emissions was expected to be strongest at the DP2050 (79.2%) and AMS01 (43.8%) sites, followed in descending order by AMS06, AMS07, and AMS18. Differences in our analysis at each of

these sites thus can be used to infer source-related differences in composition (Table 1). Comparison of HYSPLIT trajectories against corresponding continuous station data displayed a general agreement between modelled and observed wind direction between exposure periods (Figure S4). Bivariate analysis demonstrated strong positive correlations (R_S = 0.83 – 0.92) between T_{OS} and continuous pollutant species reported through WBEA (exposure average NO, NO_2, SO_2, TRS, THC; Table A1), emblematic of emission transport from OS facilities. Frequency estimates displayed weaker agreement with average $PM_{2.5}$ and CO (R_S < 0.50), likely because of the influence of non-OS sources, namely wildfire smoke.

Table 1: Summary of geographical (elevation), meteorological (wind speed, temperature, relative humidity, precipitation), air quality ($PM_{2.5}$, CO, NO, NO_2, SO_2, TRS, THC), and transport frequency (T_{OS}) variables at the co-located WBEA monitoring stations (ordered according to latitude [N to S]) during the study period (July 19–August 10, 2021). Both median and normalized median absolute deviation (%; in-parenthesis) values for each variable and station are displayed.

	AMS01	AMS06	AMS07	AMS18
Latitude	57.189428	56.751378	56.73344	55.621408
Longitude	-111.640583	-111.476694	-111.39047	-111.172686
Elevation (m)	270	362	497	673
Relative humidity (%)	70.7 (21.7)	69.8 (20.3)	71.8 (17.1)	71.3 (24.6)
Wind speed (km hr^{-1})	6.2 (46.1)	8.4 (43.1)	6.7 (44.0)	N/A
Temperature (°C)	17.5 (18.5)	17.5 (17.9)	18.3 (16.1)	16.6 (21.9)
Precipitation (mm)	45.3	N/A	N/A	48.0
$PM_{2.5}$ (µg m^{-3})	10.27 (63.8)	8.85 (61.2)	9.08 (58.6)	9.08 (55.3)
CO (ppm)	0.40 (20.0)	N/A	0.22 (22.7)	0.28 (42.9)
NO (ppb)	0.67 (25.4)	0.42 (50.0)	0.63 (68.0)	0.34 (14.7)
NO_2 (ppb)	3.28 (75.1)	1.48 (77.7)	2.23 (55.3)	0.57 (38.6)
SO_2 (ppb)	0.67 (11.9)	0.27 (37.0)	0.17 (29.4)	0.09 (77.8)
TRS (ppb)	0.54 (22.2)	0.31 (19.4)	0.13 (61.5)	0.09 (44.4)
THC (ppm)	2.11 (6.64)	1.99 (2.5)	2.09 (4.3)	1.91 (1.5)
T_{OS} (%)	43.8	22.9	12.5	0.0

3.2 Active sampler TSP summary

Throughout the study, the DP2050 sampler measured elevated concentrations of DIC, NO_3^-, SO_4^{2-}, Na, P, S, V, Fe, and Sr compared with the other study sites, while most variables (with exception of WSOC and TDN) were depressed at AMS18 (Table 2). Measured WSOC and Abs_{365} were significantly higher at the nearfield site DP2050 compared to the remaining stations (Kruskal-Wallis; α < 0.05), while MAE_{365} values were similar across all sampling locations (Kruskal-Wallis; α > 0.05). Dissolved V, Sr, S, and Na were strongly (positively) correlated (R_S > 0.77) with T_{OS} estimates, while WSOC and Abs_{365} displayed weak positive agreement (R_S ≥ 0.45) (Table A2) with T_{OS}. Both WSOC and absorbance values were occasionally elevated during individual exposures (i.e., AMS18, August 5–7, WSOC = 7.2 µg C m^{-3}, Abs_{365} = 7.7 m^{-1}) receiving limited industrial but high wildfire atmospheric transport (Figure S5), while MAE_{365} displayed limited patterns in relation to wildfire smoke events. Moreover, WSOC and Abs_{365} were moderately correlated (Spearman α < 0.05, R_S = 0.30).

Table 2: Summary of active sample variables (with corresponding MDL; ng m^{-3}) measured during the study period (July 19–Aug 10) at each monitoring location. Median (and normalized median absolute deviation in-parenthesis) for each variable and site are shown. Sampling locations are ordered according to latitude (N to S).

Analyte (ng m^{-3})	AMS01 (n = 9)	DP2050 (n = 11)	AMS06 (n = 8)	AMS07 (n = 3)	AMS18 (n = 7)	MDL (ng m^{-3})
WSOC	3907.4 (33.0)	6156.1 (21.6)	3329.2 (14.5)	7667.0 (63.7)	4091.6 (28.8)	6.3
DIC	469.7 (15.8)	1047.4 (17.3)	476.8 (25.7)	979.8 (58.7)	461.8 (41.5)	20.6
TDN	475.9 (75.8)	883.4 (42.7)	372.1 (50.2)	1569.9 (63.3)	732.9 (17.8)	1.9
NO_3^-	325.7 (55.1)	845.6 (67.3)	530.3 (67.0)	734.9 (94.5)	109.0 (44.6)	18.8
SO_4^{2-}	900.7 (58.0)	2931.8 (54.6)	1113.5 (73.5)	1275.2 (87.8)	301.2 (12.0)	3.3
Cl^-	9.8 (78.7)	74.9 (47.7)	81.7 (67.5)	79.3 (58.2)	20.2 (42.4)	2.4
Na	64.3 (46.1)	194.4 (44.5)	58.7 (85.4)	55.9 (21.4)	15.7 (44.6)	1.9
Mg	52.2 (53.5)	119.7 (25.7)	34.1 (22.3)	122.9 (77.3)	19.7 (48.0)	1.6
P	7.8 (41.7)	15.1 (12.6)	9.6 (14.5)	10.7 (79.4)	5.0 (30.1)	0.4
S	303.6 (32.1)	710.3 (51.2)	203.9 (31.0)	244.8 (30.9)	200.8 (12.8)	0.8
K	89.7 (19.8)	91.4 (42.4)	121.5 (39.6)	100.8 (51.2)	44.9 (25.7)	1.1
Ca	772.2 (76.8)	1938.4 (22.1)	592.9 (5.9)	1558.3 (87.9)	315.9 (45.1)	3.3
V	0.11 (57.9)	0.20 (30.6)	< 0.1 (78.7)	< 0.1 (78.7)	< 0.1 (69.1)	< 0.1
Cr	0.8 (58.8)	1.9 (9.2)	0.5 (62.8)	1.8 (93.5)	0.4 (9.4)	0.1
Mn	3.3 (48.9)	8.5 (30.9)	4.5 (42.5)	8.4 (70.8)	1.1 (34.8)	0.1
Fe	3.7 (44.6)	8.8 (28.6)	1.9 (50.9)	2.5 (36.2)	1.8 (34.9)	0.2
Zn	3.4 (30.8)	5.0 (80.4)	8.9 (27.8)	3.8 (34.3)	2.8 (14.5)	0.4
Sr	1.7 (60.4)	4.8 (22.2)	1.6 (77.5)	0.8 (32.1)	0.2 (191.0)	0.2
Abs_{365}[a]	4.1 (44.5)	7.5 (29.8)	3.1 (28.0)	4.5 (47.0)	3.2 (45.1)	0.2
MAE_{365}[b]	1.1 (40.0)	1.0 (45.6)	0.9 (25.7)	0.9 (23.8)	1.0 (29.6)	-

[a] Reported as m^{-1}

[b] Reported as m^{-2} g C^{-1}

3.3 Fluorescence

The EEMs produced from the TSP samples frequently displayed peak fluorescence (> 30 QSU) within the λ_{Ex} and λ_{Em} wavelength ranges of 210–350 nm and 390–430 nm, respectively. Moreover, secondary peaks (> 20 QSU) were observed within the excitation range of 200–250 nm, and emission range of 250–400 nm. Fluorescent scans of raw bitumen and dry MFT materials produced strong peaks (> 30 QSU) in the similar region of λ_{Ex} of 200-250 nm and λ_{Em} of 250-400 nm, and limited fluorescence within the higher range (λ_{Ex} of 210-350 nm and λ_{Em} of 390-430 nm) (Figure A1). Similar scans of unpaved road dust materials displayed fluorescence in the λ_{Ex} of 200-250 nm and λ_{Em} of 250-400 nm regions; however, emission intensity was weak (≤ 8 QSU).

Comparative analysis of multiple PARAFAC models indicated that a model rank of three was most appropriate, that is, the data suggest three distinct classes of organic compounds were present. The three-component model displayed a high degree of fit (0.95), CC (96.2) and split-half validation (0.87) scores. The modelled components displayed clearly defined fluorescent peaks / regions, while no distinct and/or recuring residual peaks were observed within the model output (Figure 2).

The first fluorescent component (C1) presented two emission peaks generally classified as atmospheric HULIS in BrC literature (Dey and Sarkar, 2024; Laskin et al., 2015). Several water-quality studies have associated similar peaks with fluorophores of petrogenic and anthropogenic origin (Brünjes et al., 2022; Zito et al, 2019). Component two (C2) was reflective of PRLIS aerosols (Dey and Sarkar, 2024; Dong et al., 2014; Laskin et al., 2015), while component three (C3) was identified as PRLIS BrC with spectra similar to anthropogenic (Cao et al., 2023; Yan et al., 2020), and petrogenic (Whisenhant et al., 2022) fluorescent DOM.

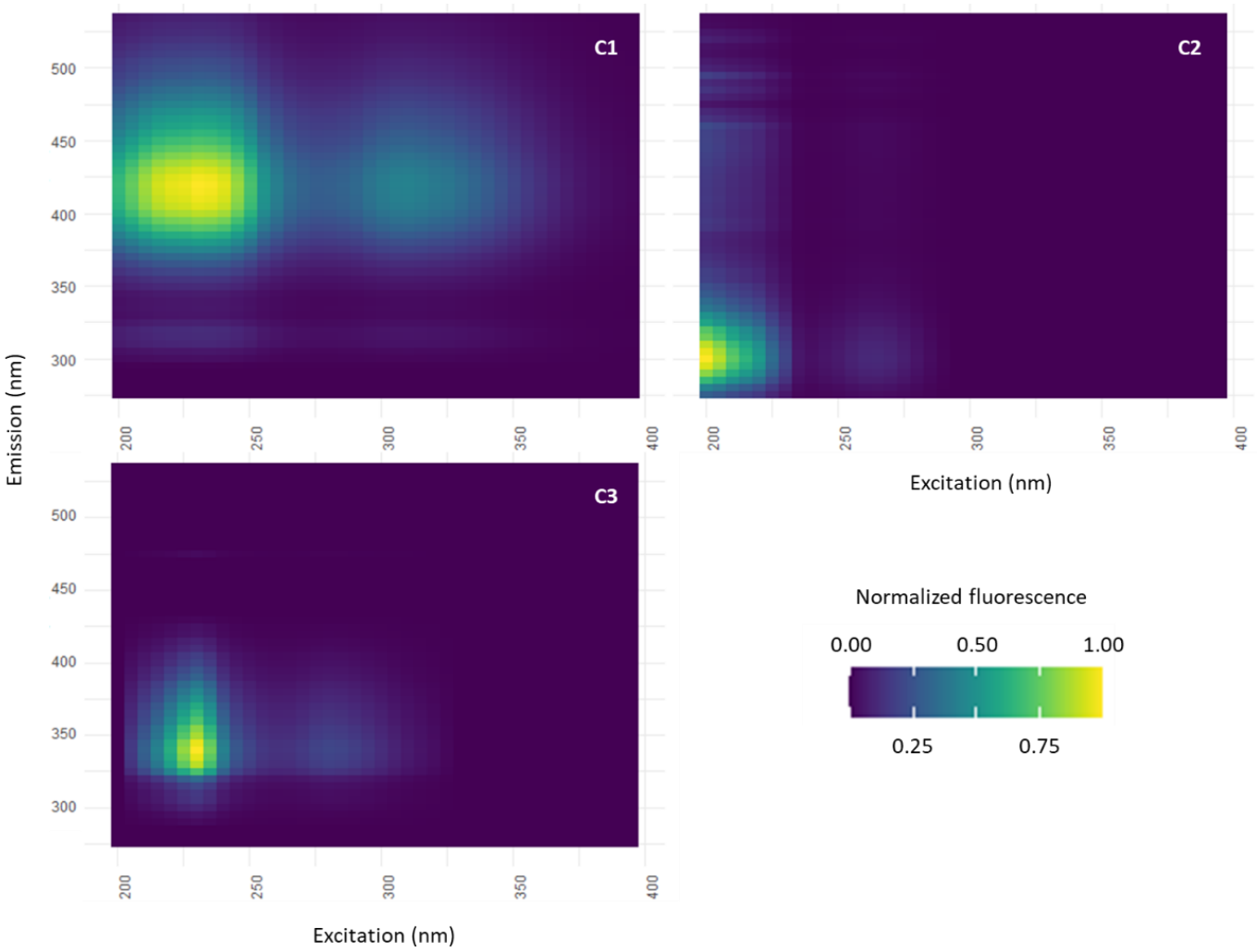

Figure 2: Visualization of the three PARAFAC components (C1–C3) generated from the combined TSP EEM sample set. Emission intensity values are normalized according to maximum component fluorescence.

Median normalized F_{MAX} (and normalized median absolute deviation, %) values for C1–C3 were 6.0 (100.0%), 34.6 (39.5%), and 10.4 (66.9%) QSU m^{-3}, respectively, demonstrating that the C2 amino acid-like component was the dominant fluorophore. The study average RPD calculated from duplicate exposures was 10.7, 8.5, and 9.6% for C1–C3, respectively. Both F_{MAX} and WSOC-normalized fluorescence (C_{WSOC}) values of C1 and C3 were highest at the near-field industrial sampling locations (DP2050, AMS01), followed by the mid-field urban sites (AMS06, AMS07), while the lowest values were reported at the background location (AMS18) (Figure 3), indicating a greater likelihood of C1, C3 having OS-related sources. Moreover, measured fluorescence at DP2050 and AMS01 was significantly higher (Kruskal-Wallis; $\alpha < 0.05$) than AMS18, further indicating that OS operations were a dominant source of C1 and C3. The second fluorescent component (C2) displayed a distinct decay in fluorescence intensity as a function of distance from OS operations. Although C2 PRLIS fluorescence was significantly elevated in DP2050 compared to all down-field sites (excluding AMS07 due to small sample size), comparison of the remaining sampling locations (including AMS18) revealed insignificant differences in measured fluorophore intensity. High relative fluorescence at the background station suggested that a broader, regional (non-OS) source contributed to C2 in the study region.

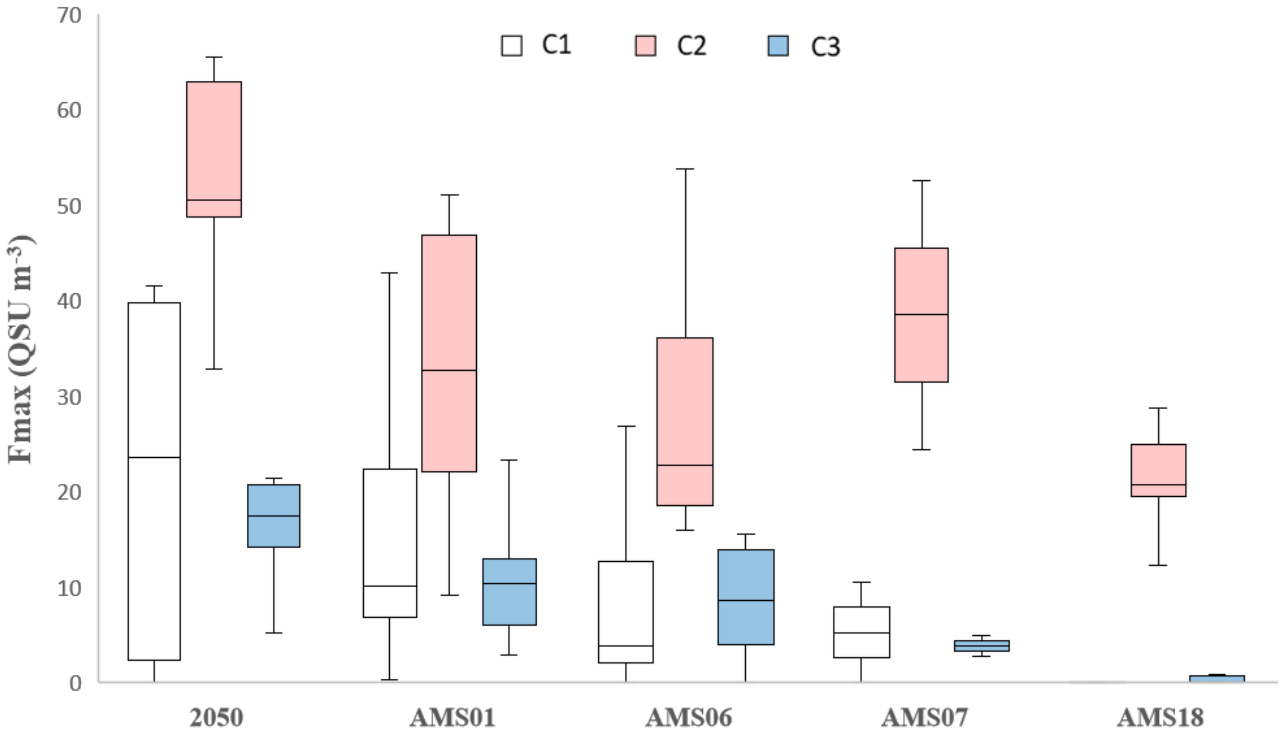

Figure 3: Distributions of component (C1–C3) fluorescence (QSU m^{-3}) measured at each sampling location during the study period (July 19–August 10).

Both C1 and C3 displayed strong positive correlations (R_S = 0.77 and 0.88, respectively) with T_{OS} (Figure 4; Table A1), suggesting fluorescence was elevated when samplers received atmospheric transport from OS operations. As specific examples, two Mildred Lake exposures (August 6–8, 8–10) with distinctly high C1 and C3 (> 100 and > 38 QSU m^{-3}, respectively) received strong SW winds (≥ 10 km h) that passed over adjacent (~1 km from site) tailings ponds, open pit mines, and active upgrading facilities (Figure 5). High F_{MAX} exposures at AMS06 between August 4–6 coincided with N-E winds passing over upwind facilities (Figure A2). Conversely, when samplers received atmospheric transport from undeveloped / forested regions, C1 and C3 were markedly lower (Figure 5). Although generally elevated when downwind of OS facilities, C2 was occasionally heightened when sites received non-industry trajectories (Figure S5). This inconsistency is reflected by the comparatively weaker correlation between T_{OS} and C2 fluorescence (R_S < 0.62). The WSOC-normalized fluorescence ($C1_{WSOC}$–$C3_{WSOC}$) displayed spatial trends relatively similar to C1–C3 (Figure A3).

Fluorescent components C1 and C3 varied independently of wildfire transport; for example, low C1 and C3 (< 0.5 and 5.2 QSU m^{-3}, respectively) were recorded during the high-smoke event at DP2050 (July19–20; Figure S5), while some of the highest F_{MAX} values were recorded during relatively smoke-free exposures at the same site (August 8–10; C1 = 137.6 QSU m^{-3}, C3 = 20.1 QSU m^{-3}). Alternatively, high C2 concentrations frequently occurred during wildfire events, where back-trajectories displayed winds originating from fire-affected regions in BC or Saskatchewan (Figure S5).

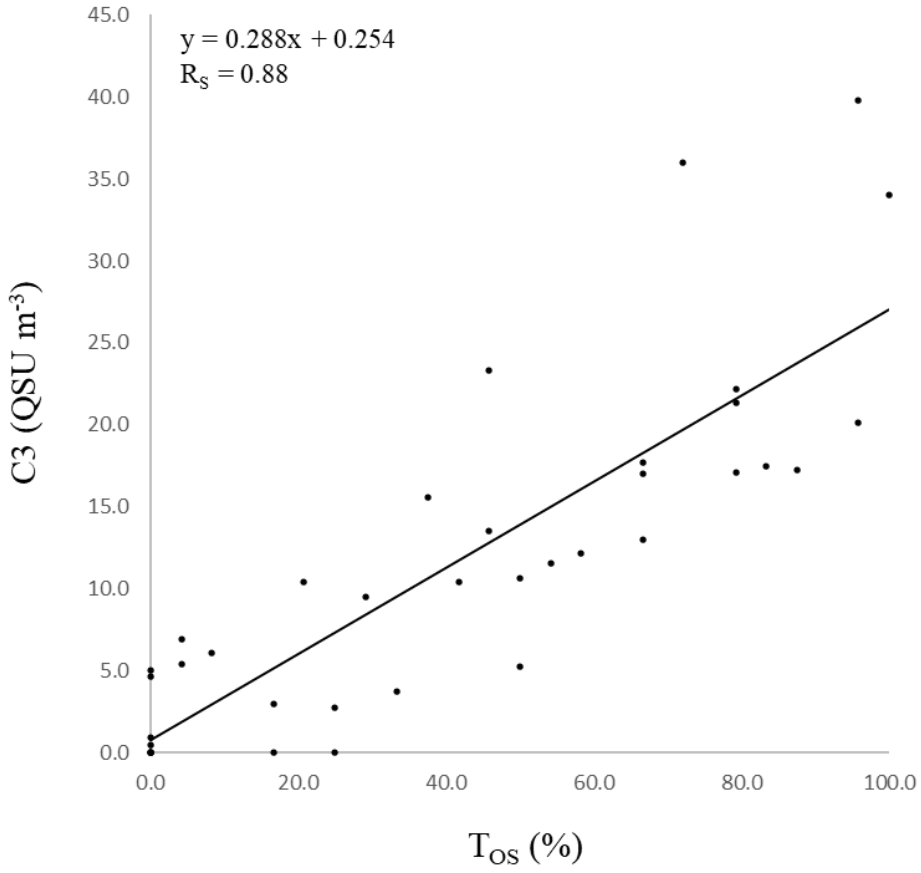

Figure 4: Bivariate comparison of active sampler measured C3 fluorescence (QSU m^{-3}) and corresponding OS trajectory frequency (T_{OS}; %) estimates throughout the study period. The line of best fit and corresponding regression equations with Pearson correlation coefficient (R_S) is displayed.

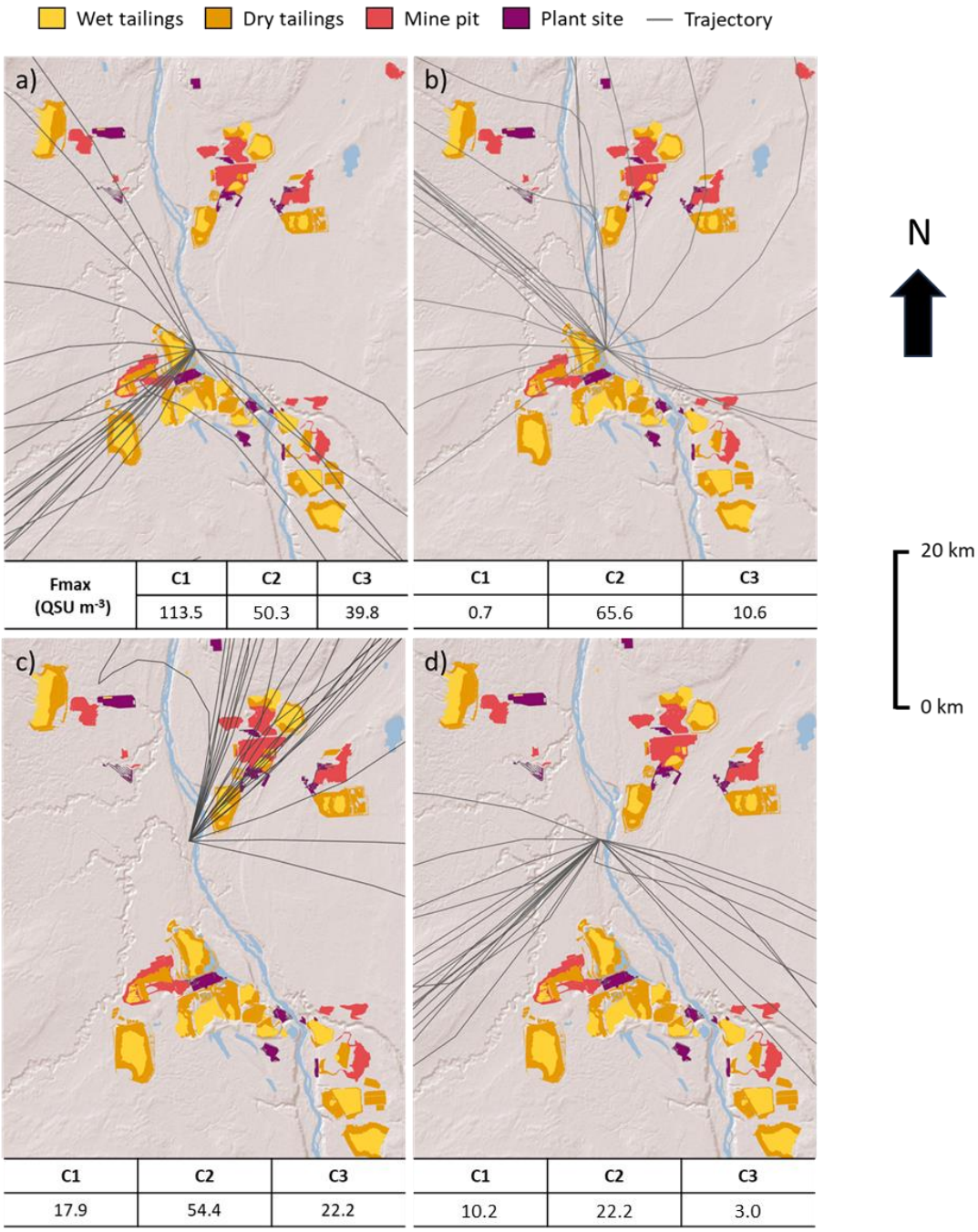

Figure 5: Spatial distributions of 48 h atmospheric back-trajectories (black lines) converging at sampling locations during selected exposure periods, including: a) DP2050; August 6–8, b) DP2050; July 29–31, c) AMS01; August 4–6 and, d) AMS01; July 21–23. Normalized F_{MAX} values of C1–C3 (QSU m^{-3}) measured during each exposure are shown beneath the corresponding trajectory plots. The spatial boundaries of various OS facilities, including wet tailings (yellow), dry tailings (orange), open mine pits (red), and plant sites (purple) are shown (© ESRI 1995-2024).

3.4 Comparison of fluorophores against supplementary TSP variables

Comparison against continuous station data found that C1 and C3 were positively correlated (Spearman; $\alpha < 0.05$) with most pollutant species (Table A1) while C2 displayed comparatively weaker correlations with continuous data. Evaluation of the complete TSP dataset found that C1 was strongly (positively) correlated ($R_s > 0.70$) with NO_3^-, SO_4^{2-}, Na, Mg, S, V, and Sr; C3

displayed similar trends, with additional correlations with Ca, P, and Mn. Moreover, C2 was moderately correlated with WSOC, DIC, Na, Mg, P, S, Ca, V, Cr, Mn, and Sr (Table A2).

Cross-validation confirmed a two-component PLS-R model that produced a relatively strong R^2Y (cumulative $R^2Y = 0.73$) and the highest cumulative Q^2Y value (0.57). The first modelled component (PLS1, $R^2Y = 0.49$) was primarily defined (VIP > 1) by NO_3^-, SO_4^{2-}, Na, Mg, P, S, Ca, V, Mn, Sr, and T_{OS}, while the second component (PLS2, $R^2Y = 0.24$) was characterized by WSOC, DIC, SO_4^{2-}, Na, P, V, and T_{OS}. Of these variables, Na and T_{OS} were the most important (VIP > 1.4) to PLS1 and PLS2. Considering certain OS fugitive emissions (e.g., tailings sand and haul road dust) are often Na enriched (Wang et al., 2015), these high VIP scores suggested both dimensions represented industrial sources. Moreover, PLS1 was positively correlated with variables previous linked to crustal (Mg, Ca, Mn) and bituminous (S, Sr, V) sources, which in the case of the AOSR could be reflective of bitumen and overburden excavation (Landis et al., 2012). Concerning PLS2, the positive correlation with Na, SO_4^{2-}, and T_{OS}, could represent non-crustal industrial sources (Wang et al., 2015), while the negative correlation with WSOC and DIC could reflect non-OS carbonaceous PM emissions. Biplot visualization revealed that C1 and C3 fluorescence were positively correlated with both PLS-R components and plotted near Na (Figure 6); both fluorophores were notably distant from WSOC and Abs_{365}. Fluorescent component 2 displayed a strong positive correlation with the first PLS-R component, and was plotted in proximity to WSOC, DIC, Ca, Mn, and Abs_{365}. Score-plot visualization of individual exposures displayed a general separation between DP2050 and the remaining sites along the first PLS-R component axis (Figure A4). The PLS-R models generated using the WSOC-normalized component fluorescence ($C1_{WSOC}$–$C3_{WSOC}$) as Y variables were comparatively weak, as a two-component model displayed low cumulative R_2Y (0.48) and Q_2Y (0.18) scores.

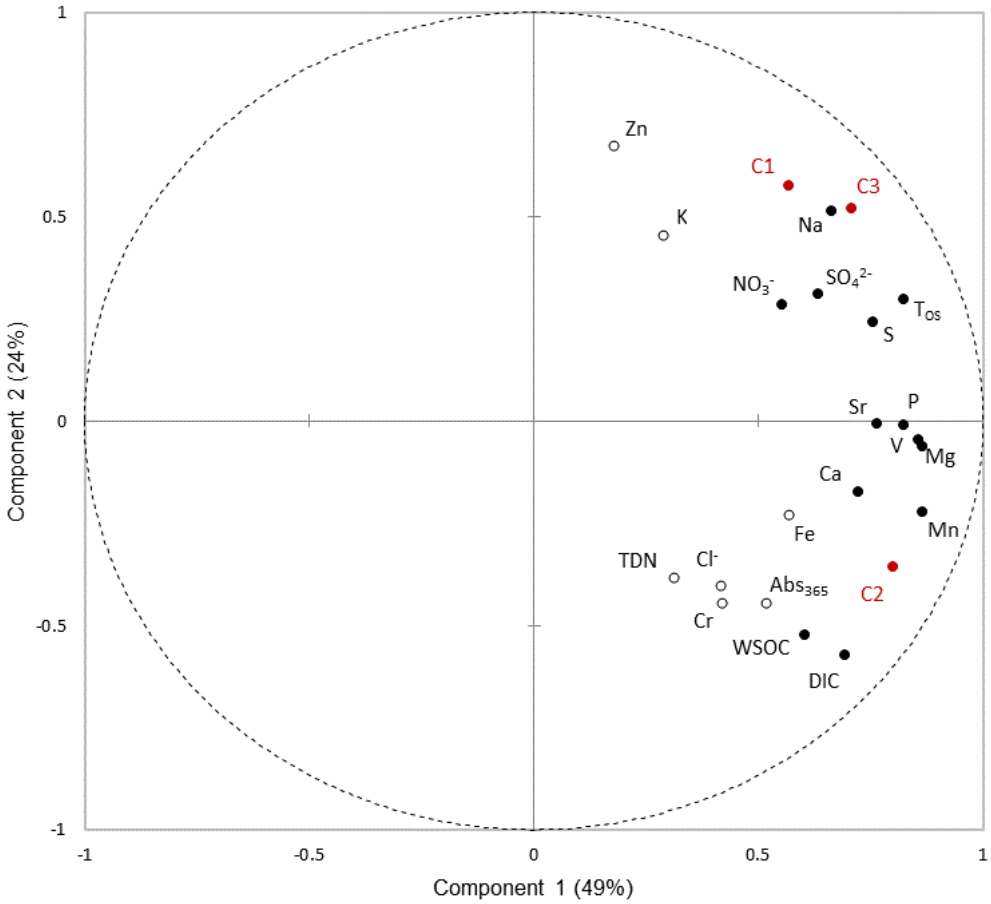

Figure 6: Correlation biplot displaying both X (black) and Y (red) variables in relation to the first two partial least square regression components. Filled and outlined black points indicate X variables assigned high (≥ 1) and low (< 1) VIP scores, respectively.

4 Discussion

4.1 WSOC and WS-BrC absorption

Ambient WSOC in the AOSR (including AMS18) were higher than TSP-based (summertime) measurements (WSOC < 1 µg C m^{-3}) from the remote southern Tibetan Plateau (Cong et al., 2015; Li et al., 2021) and Greenland Ice Sheet (Hagler et al., 2007), but similar to the magnitude of values (1–10 µg C m^{-3}) reported from Sinhagad, India (Kirillova et al., 2013), Bangkok, Thailand (Tang et al., 2021), Karachi, Pakistan (Chen et al., 2020), and peatland-fire affected samples from west Russia (Popovicheva et al., 2019). Conversely, WSOC in the AOSR was generally lower than the measured concentrations (> 10 µg C m^{-3}) in New Delhi, India (Kirillova et al., 2014; Miyazaki et al., 2009).

Compared to previous studies focused on the TSP fraction, Abs_{365} in the AOSR was generally higher than summertime values reported from remote regions including the Tibetan Plateau (Abs_{365} = 0.4 m^{-1}, Zhu et al., 2018), Gobi Desert (1.9 m^{-1}, Wen et al., 2021), and the Amazon Basin (< 1.4 m^{-1}, Saturno et al., 2018), similar to observations from Bangkok (4.5 m^{-1}, Tang et al., 2021), and smaller relative to polluted urban areas in Eastern China (8.4 m^{-1}, Wen et al., 2021). Observed MAE_{365} in the AOSR was 25 – 400% higher than the values reported across a diversity of studies (Srinivas and Sarin, 2013; Tang et al., 2021; Wu et al., 2019), demonstrating WS-BrC possessed relatively high light absorption capacity.

The moderate positive correlation between WSOC and Abs_{365} indicated that WS-BrC was an appreciable constituent of soluble organic carbon in the study region, and both TSP fractions likely shared select environmental sources. Higher WSOC and Abs_{365} values at DP2050 relative to the other study sites indicated industrial operations may contribute to regional WS-BrC; the significant positive correlation between Abs_{365} and T_{OS} further supported this assertion. However, the similarity in WSOC and Abs_{365} between the remaining stations (excluding DP2050) implied that the extent of OS influence was spatially limited, and regional sources were the primary determinant of BrC at further-field locations. Elevated WSOC and absorbance during smoke events (e.g., AMS18, August 5–7) suggested biomass combustion was a source of BrC. Regional wildfire smoke could explain why TSP-phase WSOC and Abs_{365} at the background site (AMS18) was higher than other remote areas such as the Tibetan Plateau and Greenland ice sheet (Hagler et al., 2007; Zhu et al., 2018), but comparable to WSOC concentrations during boreal fire events in west Russia (Popovicheva et al., 2019). Insignificant differences in MAE_{365} between AOSR sites, and inconsistent MAE_{365} values during extreme fire smoke events demonstrated that aerosol light absorption capacity was not dependant upon OS or wildfire sources.

4.2 C1 and C3 fluorescent components

Elevated C1 and C3 fluorescence among near-field (< 5 km) industrial sites (DP2050, AMS01), and significant positive correlations with T_{OS} and continuous pollutant data indicated that OS emissions contributed to measured fluorescence. Depressed F_{MAX} values during exposures where air masses originated from non-OS (AMS01; August 21–23) and/or background regions (i.e., AMS18) further indicated that industrial operations were the primary source of C1 and C3 in the AOSR. Moreover, low emission intensity (with exception of C2) during smoke events (DP2050, July 19-20; AMS18, August 5-7; Figure S5) demonstrated that biomass combustion was not the primary source of C1 and C3 fluorescence.

Source-apportionment studies have identified bitumen excavation and hauling as a key source of PM to the AOSR; emissions that are often associated with Na, S, and V (Landis et al., 2012; 2017). Therefore, the importance of Na and SO_4^{2-} as predictors of C1 and C3 variation could further link bitumen emissions to observed fluorescence. The spectral similarity between the raw bitumen EEM and PRLIS C3 confirmed that OS material likely contributed to at least one of the observed fluorescent peaks. Resuspended oil sands materials have been shown to significantly contribute to atmospheric loadings of total PAC species (Landis et al., 2019),

where somewhat water-soluble and low molecular weight (LMW) PACs (i.e., naphthalene, fluorene, dibenzothiophene) could fluoresce in the excitation and emission wavelength range like C1 (Driskill et al., 2018). Photodegradation of exposed bituminous material can produce oxygenated PACs (Yang et al., 2016), which due to their enhanced water solubility could additionally contribute to WS-BrC fluorescence.

Fugitive dust emissions from tailings ponds are an additional source of PM in the study region (Landis et al., 2012; 2019; Zhang et al., 2016). Owing to the application of NaOH to accelerate the crude extraction process (Bakhtiari et al., 2015), OS tailings contain high concentrations of Na (MacKinnon and Sethi, 1993; Wang et al., 2015). The strong association of Na with C1 and C3 (via PLS-R) provided evidence to suggest tailings dust contributed to observed fluorescence. Oil sands tailings dust has been identified as a source of 1–3 ring PACs and naphthenic acids (Landis et al., 2012; Yassine and Dabek-Zlotorzynska, 2017; Zhang et al., 2016), which can fluoresce in λ_{Ex} and λ_{Em} regions like C1 and C3 (Driskill et al., 2018; Kaur et al., 2014). The spectral similarity between C3 and MFT reference material, and elevated C1 and C3 emission intensity during exposures downwind of tailings-sites further implied fugitive facility emissions contributed to BrC fluorescence.

Emission source profiles previously identified in the AOSR have been shown to contain loadings indicative of both crustal (Mg, Ca, Mn) and petrogenic origin (S, V, Ni) (Landis et al., 2012), largely because of the proximity and co-emission of different dust sources associated with OS activities. The first PLS-R component, which displayed strong correlations with Mg, Ca, Mn, C1, and C3, may be broadly representative of crustal emissions (e.g., haul road dust, excavated surface-soils and overburden) from OS operations. However, separation of Mg, Ca, and Mn from C1 and C3 along the second PLS-R component (non-crustal) axis plot implied the fluorophores were co-emitted along-side these crustal sources.

Analysis of the current TSP dataset was unsuccessful in distinguishing between C1 and C3, likely indicating the co-emission of these fluorophores from industrial sources. However, unlike C3, the C1 HULIS fluorophore did not match the EEM spectra produced from the raw bitumen or MFT extracts, which suggested the two fluorophores originated from different emission sources associated with OS operations. Industrial facilities in the AOSR often contain stockpiles and beaches comprised of petroleum coke (petcoke), a carbon-rich derivative of the oil refining process that has been previously identified as a major source of particulate PAC emissions to the surrounding region (Zhang et al., 2016). Fugitive petcoke dust co-emitted from OS facilities could contribute to observed C1 fluorescence. Future BrC field studies should consider increased sampling locations near a diverse range of OS facilities, shortened exposure periods (to limit source mixing), and expanded analysis of complimentary OS indicator variables (e.g., molybdenum, nickel, PACs, [Landis et al., 2019]) to better characterize C1 and C3 source profiles in the AOSR.

4.3 C2 fluorescent component

Significant positive correlations between C2, WSOC and Abs_{365} suggested that the fluorophore was a key constituent of bulk WS-BrC in the AOSR, consistent with the observed dominance of C2 over total sample fluorescence. Significantly elevated C2 at the near-field (< 1 km) Mildred Lake site, yet comparable fluorescence at AMS18 relative to the remaining stations suggested both industrial and broad regional sources contributed to BrC across the study area, consistent with what was observed for WSOC and Abs_{365}.

Occasionally elevated fluorescence during regional smoke events (e.g., July 19-20, DP2050) indicated wildfire smoke contributed to C2 fluorescence; this is unsurprising given that biomass combustion is one of the leading sources of BrC globally (Chen and Bond, 2010). Particulate matter originating from biomass combustion can contain substantial quantities of water-soluble organic carbon (Park et al., 2013; Pastor et al., 2020), which could explain the observed association between WSOC and C2. Future

evaluations of BrC in the AOSR should additionally measure pyrogenic tracer species such as retene and levoglucosan, as these organic compounds can be used for wildfire source apportionment (Wentworth et al., 2018).

The similarity in fluorescent spectra when comparing C2 and road dust EEMs indicated the potential influence of crustal fugitive dust emissions over fluorescent PM. Haul roads throughout the AOSR are generally constructed using locally excavated limestone and bitumen, and regional road dust emission profiles often contain high loadings of DIC, Mg, Ca, and Mn (Wang et al., 2015). The observed associations (PLS-R) between these variables and C2 among the TSP samples further supported the potential influence of road dust emissions over measured fluorescence. Road dust materials can contain a diversity of chromophoric organic matter, including amino acids (Chalbot and Kavouras, 2019) and LMW PACs (in the case of hauling and industrial roads in the OS) (Landis et al., 2019) that can fluoresce in the low λ_{Ex} and λ_{Em} wavelength range like C2 (Christensen et al., 2005; Kim and Koh, 2020). Following initial suspension, larger diameter road dust particles are rapidly removed from the atmosphere through physical interactions with the surface environment (vegetation, man-made structures, etc.). For example, Veranth et al. (2003) found that irregular surface conditions adjacent to an unpaved road in Utah (United States) contributed to an 85% reduction of coarse particulate matter within 100 m of the emission source. In the case of the AOSR, industrial haul roads close to (< 1 km) site DP2050 contributed to elevated C2 fluorescence, while rapid removal further downwind possibly explained why C2 was relatively similar between the remaining downfield sites. In the absence of appreciable OS road dust influence, regional wildfire smoke likely became the dominant source of C2 fluorescence. Future studies should consider using pyrogenic (retene, levoglucosan) and petrogenic (molybdenum, nickel, PACs) indicator variables to determine the relative contribution of wildfire and OS emission sources to C2 fluorescence in the AOSR.

5 Conclusions

Optical analysis of atmospheric TSP samples collected throughout the AOSR found that OS activities were a measurable source of WS-BrC to the surrounding airshed during the summer season. Significantly higher Abs_{365} measured at the industry adjacent site (DP2050) demonstrated that OS operations likely enhanced aerosol light absorbance, which in turn could impact local solar radiation budgets and atmospheric photochemistry. However, statistically similar Abs_{365} and MAE_{365} values across the remaining stations indicated that the influence of OS emissions over WS-BrC absorbance was spatially limited and unlikely to substantially influence the regional climate during the summer. Combined EEM and PARAFAC evaluation of the TSP samples identified three distinct fluorophores (C1–C3), all of which exhibited a potential link to industrial activity. However, uniformly elevated C2 emission intensity during wildfire smoke episodes indicated biomass combustion was also a considerable source of PRLIS aerosols to the region, while C1 and C3 were predominantly linked to OS sources.

As far as the authors are aware, this is the first study to evaluate WS-BrC in the AOSR airshed. Considering the low operational costs compared to conventional methods of mass spectrometry, UV-Vis and EEM-PARAFAC offer accessible techniques to monitor WS-BrC and initially screen for OS-sourced aerosols throughout the AOSR. Moreover, the capacity of EEM-PARAFAC to identify fluorescent species strongly linked to industry suggested that similar spectroscopic techniques could be employed to evaluate WS-BrC near other oil and gas facilities worldwide.

Appendix A

Datasets were acquired using an Agilent 8800 triple quadrupole inductively coupled mass spectrometer, in the Water Quality Centre at Trent University. A MicroMist nebulizer (nominal uptake rate 400 μL min^{-1}) and Scott double pass spray chamber was used for sample introduction.

Table: Instrument operating conditions and measurement parameters.

RF power	1550 W
Carrier gas flow rate[a]	1.05 L min^{-1}
Sampling depth[a]	10 mm
Extraction lens	X-type
Sampler and skimmer cone	Standard nickel

[a] General Purpose Plasma Preset

Calibration standards were prepared by serial dilution of a 100 ng mL^{-1} multi-element solution (HPS QCS 27) and 1000 ng mL^{-1} single element standards in 2% HNO_3. High purity water (18.2 MΩ) and nitric acid was used for the preparation of all solutions. The NIST SRM 1640a (Trace Elements in Natural Water), NRC SLRS-6 (River Water Certified Reference Material for Trace Metals) and CALA PT standards were used for QA/QC. The measured concentrations were within 5% of the certified values.

Table: Instrument tune mode and scan type used to measure each element.

Element	Tune Mode	Scan Type
Na	He	Single Quad
Mg	He	Single Quad
P	O_2	MS/MS
S	O_2	MS/MS
K	H_2	MS/MS
Ca	H_2	MS/MS
V	O_2	MS/MS
Cr	He	Single Quad
Mn	He	Single Quad
Fe	H_2	MS/MS
Zn	He	Single Quad
Sr	No gas	Single Quad

Table A1. Spearman correlation analysis comparing absorbance indices (Abs_{365}, MAE_{365}), modelled fluorescent components (C1-C3), trajectory frequencies (T_{OS}), and continuous pollutant species measured at the active sampling locations (excluding 2050). The correlation coefficient (R_S) for each significant correlation (α < 0.05) is shown.

	T_{OS}	THC	TRS	SO_2	NO_2	NO	CO	$PM_{2.5}$
THC	0.87	-	-	-	-	-	-	-
TRS	0.92	0.85	-	-	-	-	-	-
SO_2	0.84	0.73	0.89	-	-	-	-	-
NO_2	0.9	0.91	0.88	0.82	-	-	-	-
NO	0.82	0.83	0.89	0.82	0.89	-	-	-
CO	0.5	0.47	0.63	0.65	0.66	0.54	-	-
$PM_{2.5}$	0.48	0.57	0.5	0.42	0.6	0.4	0.67	-
C1	0.77[a]	0.7	0.67	0.54	0.66	0.57	0.48	0.72
C2	0.62[a]	-	-	-	0.42	0.42	-	-
C3	0.88[a]	0.73	0.73	0.6	0.71	0.65	0.4	0.58
MAE_{365}	-	-	-	-	-	-	-	-
Abs_{365}	0.48[a]	-	-	-	-	0.36	-	-

[a] Correlation calculated using data from all stations, including DP2050.

Table A2: Spearman correlation analysis of modelled fluorescent components (C1-C3) against corresponding chemical and optical variables measured through the active sampler network. The coefficient (R_S) of each significant correlation ($\alpha < 0.05$) is shown.

Analyte	PARAFAC			Component / WSOC			Absorbance	
	C1	C2	C3	$C1_{WSOC}$	$C2_{WSOC}$	$C3_{WSOC}$	Abs_{365}	MAE_{365}
WSOC	-	0.70	-	-	-	-	0.55	-
DIC	-	0.80	-	-	-	-	0.57	-
TDN	-	0.44	-	-	-	-	0.39	-
NO_3^-	-	0.49	0.42	-	-	-	-	-
SO_4^{2-}	0.54	0.48	0.58	0.41	-	0.40	-	-
Cl^-	-	-	-	-	-	-	-	-
Na^+	0.62	0.61	0.75	0.57	-	0.60	0.36	-
Mg^{2+}	0.49	0.62	0.66	0.41	-	0.46	-	-
K^+	-	-	-	-	-	-	-	-
Ca^{2+}	0.35	0.74	0.57	-	-	-	0.54	-
P	-	0.71	0.55	-	-	-	0.55	-
S	0.62	0.56	0.71	0.65	0.36	0.68	-	-
V	0.52	0.65	0.69	0.39	-	0.45	0.52	-
Cr	-	0.72	-	-	-	-	0.57	-
Mn	0.37	0.63	0.57	-	-	-	-	-
Fe	0.36	0.40	0.33	-	-	-	0.42	-
Zn	-	-	-	-	-	-	-	-
Sr	0.62	0.63	0.79	0.56	0.47	0.60	0.42	-
Abs_{365}[a]	-	0.74	0.37	-	-	-	-	0.63
MAE_{365}[b]	-	-	-	-	0.57	0.36	0.63	-

[a] Reported as m^{-1}

[b] Reported as $m^{-2}gC^{-1}$

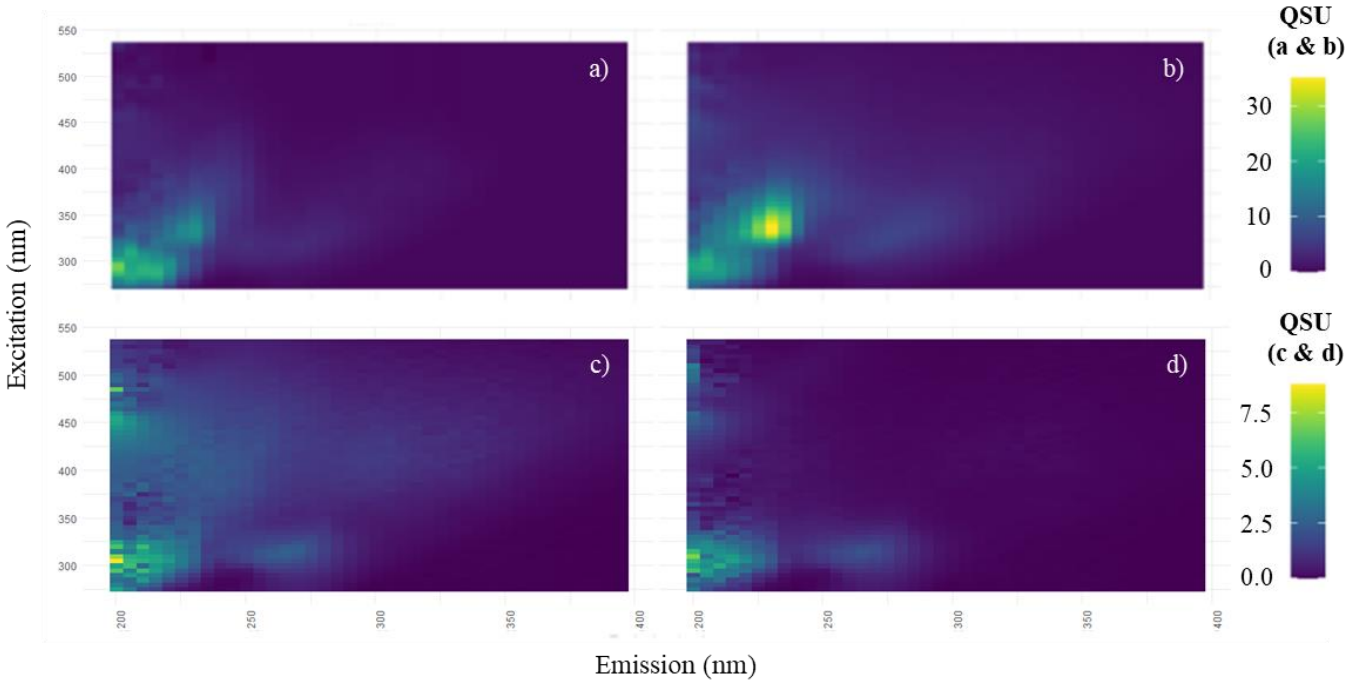

Figure A1: Visualization of the EEM scans produced from a) raw bitumen, b) dry MFT, and unpaved road dust from c) DP2050 and d) AMS01. Fluorescence intensity is displayed in QSU. Note that panels a and b follow a different colour-scale than panels c and d.

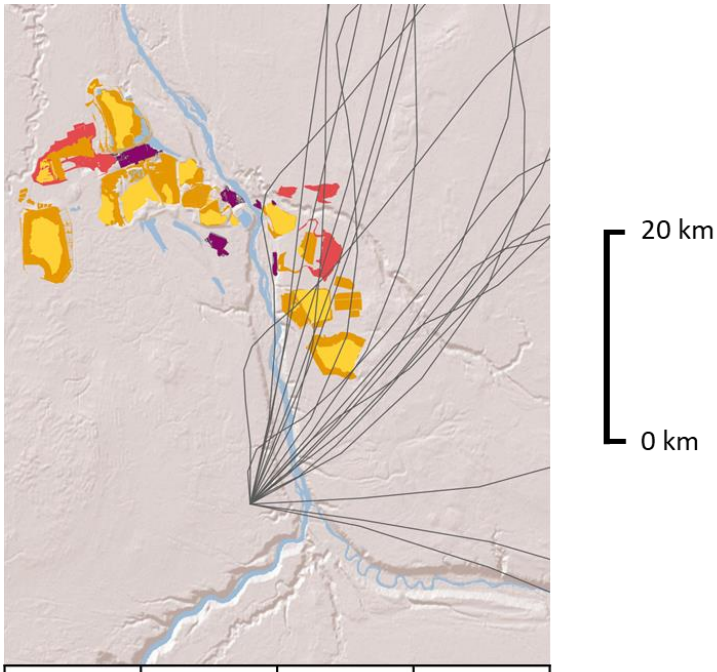

Fmax (QSU m^{-3})	C1	C2	C3
	40.7	53.9	36.0

Figure A2: Spatial distributions of 48 h atmospheric back-trajectories (black lines) converging at AMS06 during the August 4–6 exposure. F_{MAX} values of C1–C3 (QSU m^{-3}) measured during the corresponding exposure are shown. The spatial boundaries of various OS facilities, including wet tailings (yellow), dry tailings (orange), open mine pits (red), and plant sites (purple) are shown (© ESRI 1995-2024).

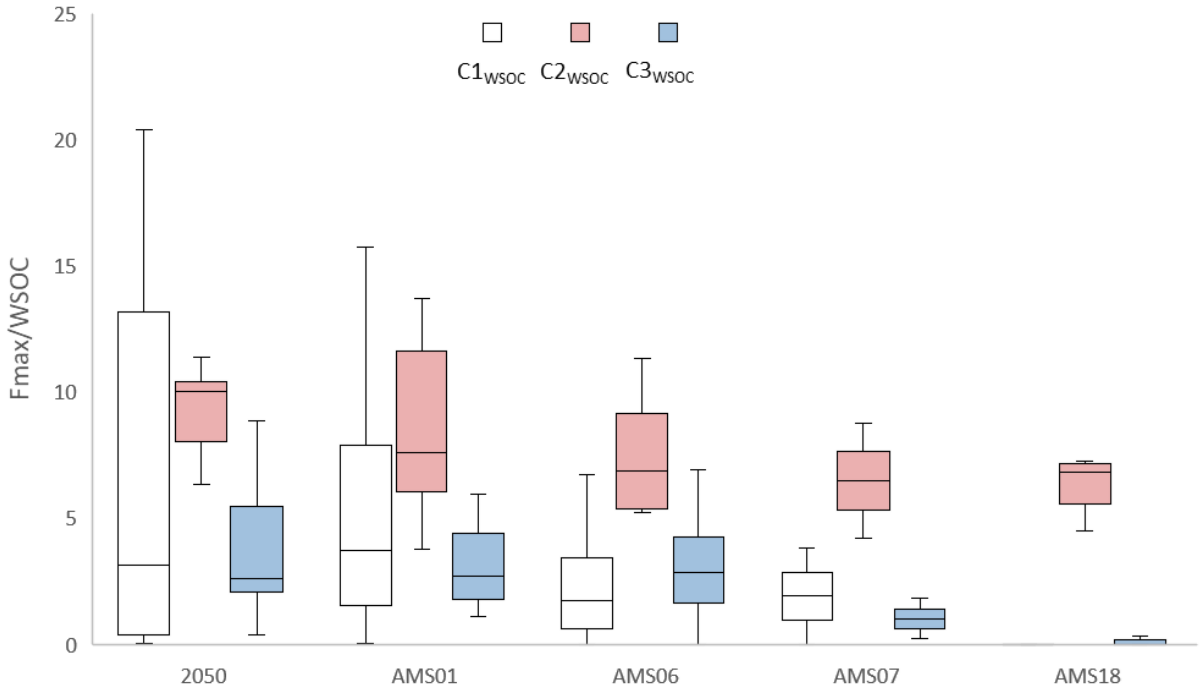

Figure A3: Distributions of WSOC - normalized component fluorescence ($C1_{WSOC}$ – $C3_{WSOC}$) measured at each sampling location during the study period (July 19 – August 10, 2021).

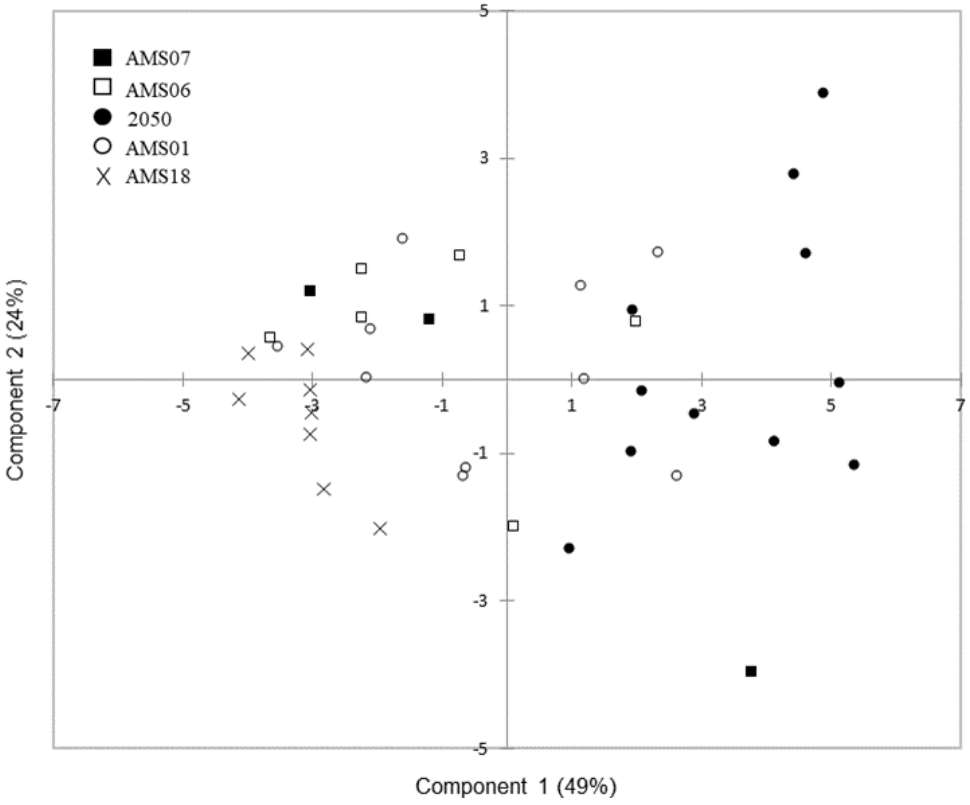

Figure A4: PLS-R Biplot displaying the distribution of observations relative to the first two modelled components. Observations are categorized according to site ID, including: AMS01 (open circle), DP2050 (full circle), AMS06 (open square), AMS07 (full square), AMS18 (x-mark).

Author contributions

Conceptualization: D.B., J.A.; Field sampling and laboratory analysis: D.B., M.G., D.H.D., J. A.; Writing original draft: D.B.; Writing review and editing: D.B., M.G., D.H.D., P.A.M., J. A

Competing interests

The authors declare that they have no conflict of interest.

Acknowledgements

This study was made possible through collaboration with the Wood Buffalo Environmental Association (Alberta, Canada), laboratory analysis by the Trent University Water Quality Center (Ontario, Canada), and research funding provided by Environment and Climate Change Canada (GCXE20S046). The primary author (D.B.) would also like to thank Mark Gordon and Timothy Jiang for their assistance in the field.

References

Arp, H. P. H., Lundstedt, S., Josefsson, S., Cornelissen, G., Enell, A., Allard A.-S., and Kleja, D. B.: Native Oxy-PAHs, N-PACs, and PAHs in Historically Contaminated Soils from Sweden, Belgium, and France: Their Soil-Porewater Partitioning Behavior, Bioaccumulation in Enchytraeus crypticus, and Bioavailability, Environ. Sci. Technol., 48, 19, 11187–11195, doi: 10.1021/es5034469, 2014.

Bakhtiari, T. M., Harbottle, D., Curran, M., Ng, S., Spence, J., Siy, R., Liu, Q., Masliyah, J., and Xu. Z.: Role of caustic addition in bitumen-clay interactions. Energy Fuels 29,1, 58–69, doi: 10.1021/ef502088z, 2015.

Bari M. A., and Kindzierski W. B.: Ambient volatile organic compounds (VOCs) in communities of the Athabasca oil sands region: Sources and screening health risk assessment. Environ. Pollut., 235:602-614, doi: 10.1016/j.envpol.2017.12.065, 2018.

Basnet, S., Hartikainen, A., Virkkula, A., Yli-Pirilä, P., Kortelainen, M., Suhonen, H., Kilpeläinen, L., Ihalainen, M., Väätäinen, S., Louhisalmi, J., Somero, M., Tissari, J., Jakobi, G., Zimmermann, R., Kilpeläinen, A., and Sippula, O.: Contribution of brown carbon to light absorption in emissions of European residential biomass combustion appliances, Atmos. Chem. Phys., 24, 3197–3215, https://doi.org/10.5194/acp-24-3197-2024, 2024.

Bro, R.: PARAFAC. Tutorial and applications. Chemom. Intell. Lab. Syst., 38,2, 149-171. doi: 10.1016/S0169-7439(97)00032-4, 1997.

Bro, R., and Kiers, H.A.: A new efficient method for determining the number of components in PARAFAC models. J. Chemom., 17, doi: 10.1002/cem.801, 2003.

Brünjes, J., Seidel, M., Dittmar, T., Niggemann, J., and Schubotz, F.: Natural Asphalt Seeps Are Potential Sources for Recalcitrant Oceanic Dissolved Organic Sulfur and Dissolved Black Carbon. Environ. Sci. Technol., 56,12, 9092-9102, doi: 10.1021/acs.est.2c01123, 2022.

Cao, T., Li, M., Xu, C., Song, J., Fan, X., Li, J., Jia, W., and Peng, P.: Technical note: Chemical composition and source identification of fluorescent components in atmospheric water-soluble brown carbon by excitation–emission matrix spectroscopy with parallel factor analysis – potential limitations and applications, Atmos. Chem. Phys., 23, 2613–2625, https://doi.org/10.5194/acp-23-2613-2023, 2023.

CCME (Canadian Council of Ministers of the Environment): Canadian Soil Quality Guidelines for Carcinogenic and Other Polycyclic Aromatic Hydrocarbons (Environmental and Human Health Effects). Scientific Criteria Document, Environment and Climate Change Canada, Gatineau, Québec, Canada, 218, 2010.

Chakrabarty, R. K., Gyawali, M., Yatavelli, R. L., Pandey, A., Watts, A. C., Knue, J., Moosmüller, H.: Brown carbon aerosols from burning of boreal peatlands: microphysical properties, emission factors, and implications for direct radiative forcing. Atmos. Chem. Phys., 16, 5, 3033-3040, 2016.

Chalbot, M-C. G., and Kavouras, I. G.: Nuclear Magnetic Resonance characterization of water-soluble organic carbon of atmospheric aerosol types. Nat. Prod. Commun., 14,5, doi: 10.1177/1934578X19849972, 2019.

Chen, Y., and Bond, T. C.: Light absorption by organic carbon from wood combustion. Atmos. Chem. Phys., 10,4, 1773– 1787, doi: 10.5194/acp-10-1773-2010, 2010.

Chen, P., Kang, S., Gul, C., Tripathee, L., Wang, X., Hu, Z., Li, C., and Pu, T.: Seasonality of carbonaceous aerosol composition and light absorption properties in Karachi, Pakistan. J. Environ. Sci., 90, 286-296, doi: 10.1016/j.jes.2019.12.006, 2020.

Chen, Q., Mu, Z., Song, W., Wang, Y., Yang, Z., Zhang, L., and Zhang, Y.-L.: Size-resolved characterization of the chromophores in atmospheric particulate matter from a typical coal-burning city in China. J. Geophys. Res. Atmos., 124, 10546– 10563, doi: 10.1029/2019JD031149, 2019.

Christensen, J. H., Hansen, A. B., Mortensen, J., and Anderson, O.: Characterization and matching of oil samples using fluorescence spectroscopy and parallel factor analysis. Anal. Chem., 77, 2210 – 2217, doi: 10.1021/ac048213k, 2005.

Claeys, M., Vermeylen, R., Yasmeen, F., Gomez-Gonzalez, Y., Chi, X. G., Maenhaut, W., Meszaros, T., and Salma, I.: Chemical characterisation of humic-like substances from urban, rural and tropical biomass burning environments using liquid chromatography with UV/vis photodiode array detection and electrospray ionisation mass spectrometry. Environ. Chem., 9, 273, doi: 10.1071/EN11163, 2012.

Cong, Z., Kang, S., Kawamura, K., Liu, B., Wan, X., Wang, Z., Gao, S., and Fu. P.: Carbonaceous aerosols on the south edge of the Tibetan Plateau: concentrations, seasonality and sources. Atmos. Chem. Phys., 15 (3),1573-1584, doi: 10.5194/acp-15-1573-2015, 2015.

Deng, J., Ma, H., Wang, X., Zhong, S., Zhang, Z., Zhu, J., Fan, Y., Hu, W., Wu, L., Li, X., Ren, L., Pavuluri, C. M., Pan, X., Sun, Y., Wang, Z., Kawamura, K., and Fu, P.: Measurement report: Optical properties and sources of water-soluble brown carbon in Tianjin, North China – insights from organic molecular compositions, Atmos. Chem. Phys., 22, 6449–6470, doi: 10.5194/acp-22-6449-2022, 2022.

Dey, S., and Sarkar, S.: Compositional and optical characteristics of aqueous brown carbon and HULIS in the eastern Indo-Gangetic Plain using a coupled EEM PARAFAC, FT-IR and 1H NMR approach. Sci. Total Environ., 921, 171084, 10.1016/j.scitotenv.2024.171084, 2024.

Dong, Z., Pavuluri, C. M., Li, P., Xu, Z., Deng, J., Zhao, X., Zhao, X., Fu, P., and Liu, C.-Q.: Measurement report: Optical characterization, seasonality, and sources of brown carbon in fine aerosols from Tianjin, North China: year-round observations, Atmos. Chem. Phys., 24, 5887–5905, https://doi.org/10.5194/acp-24-5887-2024, 2024.

Driskill, A. K., Alvey, A., Dotson, A. D., and Tomco, P. L.: Monitoring polycyclic aromatic hydrocarbon (PAH) attenuation in Arctic waters using fluorescence spectroscopy, Cold Reg. Sci. Technol., 145, 76-85, doi: 10.1016/j.coldregions.2017.09.014, 2018.

Duarte, R. M. B. O., Santos, E. B. H., Pio, C. A., and Duarte, A. D-C. : Comparison of structural features of water-soluble organic matter from atmospheric aerosols with those of aquatic humic substances. Atmos. Environ., 41, 8100-8113, doi: 10.1016/j.atmosenv.2007.06.034, 2007.

Environment and Climate Change Canada (ECCC): Historical Data; Government of Canada. http://climate.weather.gc.ca/climate_normals/results_1981_2010_e.html?stnID=402&dCode=&dispBack=1, 2024

Eriksson, L., Byrne, T., Johansson, E., Trygg, J., and Vikström, C.: Multi- and Megavariate Data Analysis Basic Principles and Applications (3rd ed, Vol. 1). Umetrics Academy, 2013.

Frank, R. A., Kavanagh, R., Burnison, B. K., Arsenault, G., Headley, J. V., Peru, K. M., Van Der Kraak, G., and Solomon, K. R. (2008). Toxicity assessment of collected fractions from an extracted naphthenic acid mixture, Chemosphere, 72, 1309–1314, doi: 10.1016/j.chemosphere.2008.04.078, 2008.

Frysinger, G. S., Gaines, R. B., Xu, L., and Reddy, C. M.: Resolving the Unresolved Complex Mixture in Petroleum-Contaminated Sediments. Environ. Sci. Technol., 37,8, 1653-1662, doi: 10.1021/es020742n, 2003.

Giesy, J. P., Ansderson, J. C., and Wiseman, S. B.: Alberta oil sands development. PNAS: Commentary, 107,3, 951-952, doi: 10.1073/pnas.0912880107, 2010.

Guan, S., Wong, D. C., Gao, Y., Zhang, T., Pouliot, G.: Impact of wildfire on particulate matter in the southeastern United States in November 2016, Sci. Total Environ., 724, 138354, doi: 10.1016/j.scitotenv.2020.138354, 2020.

Gustafsson, Ö., Kruså, M., Zencak, Z., Sheesley, R. J., Granat, L., Engström, E., Rodhe. H. Brown clouds over South Asia: biomass or fossil fuel combustion? Science, 323, 5913, 495-49833, 2009.

Hagler, G., Bergin, M., Smith, E., and Dibb, J.: A summer time series of particulate carbon in the air and snow at Summit, Greenland. J. Geophys. Res.. 112, doi: 10.1029/2007JD008993, 2007.

Harsha, M. L., Redman, Z. C., Wesolowski, J., Podgorski, D. C., and Tomco, P. L.: Photochemical formation of water soluble oxyPAHs, naphthenic acids, and other hydrocarbon oxidation products from Cook Inlet, Alaska crude oil and diesel in simulated seawater spills. Environ. Sci. Adv., 2, 447-461, doi: 10.1039/D2VA00325B, 2023.

Jariyasopit, N., Harner, T., Wu, D., Williams, A., Halappanavar, S., and Su, K.: Mapping indicators of toxicity for polycyclic aromatic compounds in the atmosphere of the Athabasca oil sands region, Environ. Sci. Technol, 50, 11282–11291, doi: 10.1021/acs.est.6b02058, 2016.

Jariyasopit, N., Harner, T., Shin, C., and Park, R.:The effects of plume episodes on PAC profiles in the Athabasca Oil Sands Region. Environ. Pollut., 282, 117014, doi: 10.1016/j.envpol.2021.117014, 2021.

Josefsson, S., Arp, H. P. H., Kleja, D. B., Enell, A., and Lundstedt, S.: Determination of polyoxymethylene (POM) – water partition coefficients for oxy-PAHs and PAHs, Chemosphere, 119, 1268–1274, doi: 10.1016/j.chemosphere.2014.09.102, 2015.

Jiang, X., Wiedinmyer, C., and Carlton, A. G.: Aerosols from Fires: An Examination of the Effects on Ozone Photochemistry in the Western United States. Environ. Sci. Technol., 46, 11878, doi: 10.1021/es301541k, 2012.

Kakumanu, M.L., Ma, L. and Williams, M.A.: Drought-induced soil microbial amino acid and polysaccharide change and their implications for C-N cycles in a climate change world. Sci. Rep., 9, 10968, doi: 10.1038/s41598-019-46984-1, 2019.

Kaur, K., Bhattacharjee, S., Pillai, R. G., Ahmed, S., and Azmi, S.: Peptide arrays for detecting naphthenic acids in oil sands process affected waters. RSC Advances, 105, 60694-60701, doi: 10.1039/C4RA10981C, 2014.

Kim, K. H., Jahan, S. A., Kabir, E., and Brown, R. J.: A review of airborne polycyclic aromatic hydrocarbons (PAHs) and their human health effects, Environ. Int., 60, 71–80, doi: 10.1016/j.envint.2013.07.019, 2013.

Kim, E. A., and Koh, B.: Utilization of road dust chemical profiles for source identification and human health impact assessment. Sci. Rep., 10,1, 14259, doi: 10.1038/s41598-020-71180-x, 2020.

Kirillova E. N., Andersson, A., Sheesley, R. J., Krusa, M., Praveen, P. S., Budhavant, K., Safai, P. D., Rao, P. S. P., and Gustafsson, Ö.: 13C- and 14C-based study of sources and atmospheric processing of water-soluble organic carbon (WSOC) in South Asian aerosols. J. Geophys. Res. Atmos., 118, 614 – 626, doi: 10.1002/jgrd.50130, 2013.

Kirillova, E. N., A. Andersson, S. Tiwari, A. K. Srivastava, D. S. Bisht, and Ö. Gustafsson.: Water-soluble organic carbon aerosols during a full New Delhi winter: Isotope-based source apportionment and optical properties, J. Geophys. Res. Atmos., 119, 3476–3485, doi: 10.1002/2013JD020041, 2014.

Kothawala, D., Stedmon, C., Müller, R., Weyhenmeyer, G., Köhler, S., and Tranvik, L.: Controls of dissolved organic matter quality: evidence from a large-scale boreal lake survey. Glob. Change Biol., 20,4, 1101-1114, 10.1111/gcb.12488, 2014.

Lakowicz, R. R. Principles of Fluorescence Spectroscopy, Springer-Verlag, New York, USA, 3rd edn., 2006

Landis, M. S., Pancras, J. P., Graney, J. R., Stevens, R. K., Percy, K. E., and Krupa, S.: Receptor Modeling of Epiphytic Lichens to Elucidate the Sources and Spatial Distribution of Inorganic Air Pollution in the Athabasca Oil Sands Region. Develop. Environ. Sci., 427–467, doi: 10.1016/B978-0-08-097760-7.00018-4, 2012.

Landis, M. S., Pancras, J. P., Graney, J. R., White, E. M., Edgerton, E. S., Legge, A., and Percy., K. E.: Source apportionment of ambient fine and coarse particulate matter at the Fort McKay community site, in the Athabasca Oil Sands Region, Alberta, Canada. Sci. Total Environ., 584–585, 105-117, doi: 10.1016/j.scitotenv.2017.01.110, 2017.

Landis, M. S., Studabaker, W. B., Pancras, J. P., Graney, J. R., Puckett, K., White, E. M., and Edgerton, E. S.: Source apportionment of an epiphytic lichen biomonitor to elucidate the sources and spatial distribution of polycyclic aromatic hydrocarbons in the Athabasca Oil Sands Region, Alberta, Canada. Sci. Total Environ., 654, 1241-1257, doi: 10.1016/j.scitotenv.2018.11.131, 2019.

Lanzerstorfer C, and Logiewa A.: The upper size limit of the dust samples in road dust heavy metal studies: Benefits of a combined sieving and air classification sample preparation procedure. Environ. Pollut., 245:1079-1085, doi: 10.1016/j.envpol.2018.10.131, 2019.

Laskin, A., Laskin, J., and Nizkorodov. S. A.: Chemistry of atmospheric brown carbon. Chem. Rev., 115,10, 4335-4382, doi: 10.1021/cr5006167, 2015.

Lemieux, C. L., Lambert, I. B., Lundstedt, S., Tysklind, M., and White, P. A.: Mutagenic hazards of complex polycyclic aromatic hydrocarbon mixtures in contaminated soil, Environ. Toxicol. Chem., 27, 978–990, doi: 10.1897/07-157.1, 2008.

Li, C., Hu, Y., Zhang, F., Chen, J., Ma, Z., Ye, X., Yang, X., Wang, L., Tang, X., Zhang, R., Mu, M., Wang, G., Kan, H., Wang, X., and Mellouki, A.: Multi-pollutant emissions from the burning of major agricultural residues in China and the related health-economic effects, Atmos. Chem. Phys., 17, 4957–4988, https://doi.org/10.5194/acp-17-4957-2017, 2017.

Li, Y., Yan, F., Kang, S., Zhang, C., Chen, P., Hu, Z., and Li, C.: Sources and light absorption characteristics of water-soluble organic carbon (WSOC) of atmospheric particles at a remote area in inner Himalayas and Tibetan Plateau, Atmos. Res., 253, 105472, doi: 10.1016/j.atmosres.2021.105472, 2021.

Liggio, J., Li, SM., Hayden, K., Taha, Y. M., Stroud, C., Darlington, A., Drollette, B. D., Gordon, M., Lee, P., Liu, P., Leithead, A., Moussa, S. G., Wang, D., O'Brien, J., Mittermeier, R. L., Brook, J. R., Lu, G., Staebler, R. M., Han, Y., Tokarek, T. W., Osthoff, H. D., Makar, P. A., Zhang, J., Plata, D. L., and Gentner D. R.: Oil sands operations as a large source of secondary organic aerosols. Nature, 534, 91–94, doi: 10.1038/nature17646, 2016.

Liggio, J., Moussa, S. G., Wentzell, J., Darlington, A., Liu, P., Leithead, A., Hayden, K., O'Brien, J., Mittermeier, R. L., Staebler, R., Wolde, M., and Li, S.-M.: Understanding the primary emissions and secondary formation of gaseous organic acids in the oil sands region of Alberta, Canada, Atmos. Chem. Phys., 17, 8411–8427, doi: 10.5194/acp-17-8411-2017, 2017.

Lin, P., Rincon, A. G., Kalberer, M., and Yu, J. Z.: Elemental Composition of HULIS in the Pearl River Delta Region, China: Results Inferred from Positive and Negative Electrospray High Resolution Mass Spectrometric Data. Environ. Sci. Technol., 46, 7454, doi: 10.1021/es300285d, 2012.

Liu, J., Scheuer, E., Dibb, J., Diskin, G. S., Ziemba, L. D., Thornhill, K. L., Anderson, B. E., Wisthaler, A., Mikoviny, T., Devi, J. J., Bergin, M., Perring, A. E., Markovic, M. Z., Schwarz, J. P., Campuzano-Jost, P., Day, D. A., Jimenez, J. L., and Weber, R. J.: Brown carbon aerosol in the North American continental troposphere: sources, abundance, and radiative forcing, Atmos. Chem. Phys., 15, 7841–7858, https://doi.org/10.5194/acp-15-7841-2015, 2015.

Lundstedt, S., White, P. A., Lemieux, C. L., Lynes, K. D., Lambert, I. B., Öberg, L., Haglund, P., and Tysklind, M.: Sources, Fate, and Toxic Hazards of Oxygenated Polycyclic Aromatic Hydrocarbons (PAHs) at PAH- contaminated Sites, Ambio, 36, 475–485, doi: 10.1579/0044-7447(2007)36[475:sfatho]2.0.co;2, 2007.

Ma, H., Li, J.,Wan, C., Liang, Y., Zhang, X., Dong, G., Hu, L., Yang, B., Zeng, X., Su, T., Lu, S., Chen, S., Khorram, M. S., Sheng, G., Wang, X., Mai, B., Yu, Z., and Zhang, G.: Inflammation Response of Water-Soluble Fractions in Atmospheric Fine Particulates: A Seasonal Observation in 10 Large Chinese Cities. Environ. Sci. Technol., 53, 3782−3790, doi: 10.1021/acs.est.8b05814, 2019.

Mamun, A. A, Celo, V., Dabek-Zlotorzynska, E., Charland, J-P., Cheng, I., and Zhang, L.: Characterization and source apportionment of airborne particulate elements in the Athabasca oil sands region, Sci. Total Environ., 788,147748, doi: 10.1016/j.scitotenv.2021.147748, 2021.

MacKinnon, M., and Sethi, A.: A comparison of the physical and chemical properties of the Tailings ponds at the Syncrude and Suncor oil sands plants, Proceedings of Fine Tailings Symposium, Oil Sands- Our Petroleum Future Conference, April 4-7, Edmonton, Alberta, Canada, 1993

Marentette, J. R., Frank, R. A., Bartlett, A. J., Gillis, P. L., Hewitt, L. M., Peru, K. M., Headley, J. M., Brunswick, P., Shang, D., and Parrott, J. L.: Toxicity of naphthenic acid fraction components extracted from fresh and aged oil sands process-

affected waters, and commercial naphthenic acid mixtures, to fathead minnow (Pimephales promelas) embryos, Aquat. Toxicol., 164, 108–117, 10.1016/j.aquatox.2015.04.024, 2015.

Miyazaki, Y., Aggarwal, S. G., Singh, K., Gupta, P. K., and Kawamura, K.: Dicarboxylic acids and water-soluble organic carbon in aerosols in New Delhi, India, in winter: Characteristics and formation processes, J. Geophys. Res., 114, D19206, doi: 10.1029/2009JD011790, 2009.

Murphy, K., Stedmon, C., Wenig, P., and Bro, R.: OpenFluor—A spectral database of auto-fluorescence by organic compounds in the environment. Anal. Meth., 6, 658, doi: 10.1039/c3ay41935e, 2014.

Park, S-S., Sim, S. Y., Bae, M-S., and Schauer. J. J.: Size distribution of water-soluble components in particulate matter emitted from biomass burning, Atmos. Environ., 73, 62-72, doi: 10.1016/j.atmosenv.2013.03.025, 2013.

Pastor, R. P., Salvador, P., Alonso, S. G., Alastuey, A., Santos, S. G. D., Querol, X., Artíñano, B.: Characterization of organic aerosol at a rural site influenced by olive waste biomass burning, Chemosphere, 248, 125896, doi: 10.1016/j.chemosphere.2020.125896, 2020

Popovicheva, O. B., Engling, G., Ku, I-T., Timofeev, M. A., and Shonija, N. K.: Aerosol emissions from long-lasting smoldering of boreal peatlands: chemical composition, markers, and microstructure. Aerosol Air Qual. Res., 19, 484-503, doi: 10.4209/aaqr.2018.08.0302, 2019.

Pucher, M., Flödl, P., Graeber, D., Felsenstein, K., Hein, T., and Weigelhofer, G.: Complex interactions of in-stream dissolved organic matter and nutrient spiralling unravelled by Bayesian regression analysis. Biogeosci., 18,10, 3103-3122, doi: 10.5194/bg-18-3103-2021, 2021.

Saturno, J., Holanda, B., Pöhlker, C., Ditas, F., Wang, Q., Moran Z. D., F. de Brito, J., Carbone, S., Cheng, Y., Chi, X., Ditas (née Katzwinkel), J., Hoffmann, T., Hrabe de Angelis, I., Könemann, T., Lavrič, J., Ma, N., Ming, J., Paulsen, H., Pöhlker, M., and Andreae, M.: Black and brown carbon over central Amazonia: Long-term aerosol measurements at the ATTO site. Atmos. Chem. Phys., 18, 17, 12817-12843, doi: 10.5194/acp-18-12817-2018, 2018.

Small, C. C., Cho, S., Hashisho, Z., and Ulrich, A. C.: Emissions from oil sands tailings ponds: Review of tailings pond parameters and emission estimates, J. Pet. Sci. Eng., 127, 490–501, doi: 10.1016/j.petrol.2014.11.020, 2015.

Spranger, T., Pinxteren, D. V., and Herrmann, H.: Atmospheric “HULIS” in Different Environments: Polarities, Molecular Sizes, and Sources Suggest More Than 50% Are Not “Humic-like”. ACS Earth Space Chem., 4,2, 272-282, doi: 10.1021/acsearthspacechem.9b00299, 2020.

Srinivas, B., and Sarin. M. M.: Light-absorbing organic aerosols (brown carbon) over the tropical Indian Ocean: impact of biomass burning emissions, Environ. Res. Lett., 8, doi: 10.1088/1748-9326/8/4/044042, 2013.

Stedmon, C.A., and Nelson, N.B.: The optical properties of DOM in the ocean. In Biogeochemistry of Marine Dissolved Organic Matter, 2nd ed.; Hansell, D., Carlson, C., Eds.; Academic Press: San Diego, CA, USA; 481–508, doi: 10.1016/B978-0-12-405940-5.00010-8, 2015.

Stedmon, C. A., Markager, S., and Bro, R.: Tracing Dissolved Organic Matter in Aquatic Environments Using a New Approach to Fluorescence Spectroscopy. Mar. Chem., 82, 239-254, doi: 10.1016/S0304-4203(03)00072-0, 2003.

Stein, A.F., Draxler, R.R, Rolph, G.D., Stunder, B.J.B., Cohen, M.D., and Ngan, F.: NOAA's HYSPLIT atmospheric transport and dispersion modeling system, Bull. Am. Meteorol. Soc., 96, 2059-2077, doi: 10.1175/BAMS-D-14-00110.1, 2015.

Stone, E. A., Hedman, C. J., Sheesley, R. J., Shafer, M. M., and Schauer, J. J.: Investigating the chemical nature of humic-like substances (HULIS) in North American atmospheric aerosols by liquid chromatography tandem mass spectrometry. Atmos. Environ., 43, 4205, doi: 10.1016/j.atmosenv.2009.05.030, 2009.

Sui, X., Wu, Z., Lin, C., and Zhou, S.: Terrestrially derived glomalin-related soil protein quality as a potential ecological indicator in a peri-urban watershed. Environ. Monit. Assess., 189,7, doi: 10.1007/s10661-017-6012-5, 2017.

Tang, J., Wang, J., Zhong, G., Jiang, H., Mo, Y., Zhang, B., Geng, X., Chen, Y., Tang, J., Tian, C., Bualert, S., Li, J., and Zhang, G.: Measurement report: Long-emission-wavelength chromophores dominate the light absorption of brown carbon in aerosols over Bangkok: impact from biomass burning, Atmos. Chem. Phys., 21, 11337–11352, doi: 0.5194/acp-21-11337-2021, 2021.

Trubetskoj, O. A, Richard, C., Voyard, G., Marchenkov V.V., and Trubetskaya, O. E.: Molecular size distribution of fluorophores in aquatic natural organic matter: application of HPSEC with multi-wavelength absorption and fluorescence detection following LPSEC-PAGE fractionation. Environ. Sci. Technol., 52,9, 5287–5295, doi: 10.1021/acs.est.7b03924, 2018.

Veranth, J. M., Pardyjak, E. R., Seshardi.: Vehicle-generated fugitive dust transport: analytic models and field study, Atmos. Environ. 37, 16, 2295-2303, doi: 10.1016/S1352-2310(03)00086-4, 2003.

Veselovskii, I., Hu, Q., Goloub, P., Podvin, T., Korenskiy, M., Pujol, O., Dubovik, O., and Lopatin, A.: Combined use of Mie–Raman and fluorescence lidar observations for improving aerosol characterization: feasibility experiment, Atmos. Meas. Tech.., 13, 6691–6701, doi: 10.5194/amt-13-6691-2020, 2020.

Wang, X., Chow, J. C., Kohl, D. D., Percy, K. E., Legge, A. H., and Watson, J. G.: Characterization of PM2.5 and PM10 fugitive dust source profiles in the Athabasca Oil Sands Region, J. Air Waste Manag. Assoc., 65, 12, 1421-1433, doi: 10.1080/10962247.2015.1100693, 2015.

Wang, X., Chow, J. C., Kohl, S. D., Percy, K. E., Legge, A. H., and Watson, J. G.: Real-world emission factors for Caterpillar 797B heavy haulers during mining operations. Particuology, 28, 22–30, doi: 10.1016/j.partic.2015.07.001, 2016.

Wen, H., Zhou, Y., Xu, X., Wang, T., Chen, Q., Chen, Q., Li, W., Wang, Z., Huang, Z., Zhou, T., Shi, J., Bi, J., Ji, M., and Wang. X.: Water-soluble brown carbon in atmospheric aerosols along the transport pathway of Asian dust: Optical properties, chemical compositions, and potential sources. Sci. Total Environ., 789,147971, doi: 10.1016/j.scitotenv.2021.147971, 2021.

Wentworth, G. R., Aklilu, Y. A., Landis, M. S., Hsu, Y. M.: Impacts of a large boreal wildfire on ground level atmospheric concentrations of PAHs, VOCs and ozone, Atmos. Environ., 178, 19-30, doi: 10.1016/j.atmosenv.2018.01.013, 2018

Whisenhant, E. A., Zito, P., Podgorski, D. C., McKenna, A. M., Redman, Z. C., and Tomco P. L.: Unique Molecular Features of Water-Soluble Photo-Oxidation Products among Refined Fuels, Crude Oil, and Herded Burnt Residue under High Latitude Conditions, ACS ES T Water, 2, 6, 994-1002, doi: 10.1021/acsestwater.1c00494, 2022.

Wu, G., Ram, K., Fu, P., Wang, W., Zhang, Y., Liu, X., Stone, E. A., Pradhan, B. B., Dangol, P. M., Panday, A. K., Wan, X., Bai, Z., Kang, S., Zhang, Q., and Cong, Z.: Water-Soluble Brown Carbon in Atmospheric Aerosols from Godavari (Nepal), a Regional Representative of South Asia. Environ. Sci. Technol., 53, 7, 3471-3479, doi: 10.1021/acs.est.9b00596, 2019.

Yan, C., Zheng, M., Desyaterik, Y., Sullivan, A. P., Wu, Y., and Collett, J. L.: Molecular characterization of water-soluble brown carbon chromophores in Beijing, China. J. Geophys. Res. Atmos., 125, e2019JD032018, doi: 10.1029/2019JD032018, 2020.

Yang, Z., Hollebone, B.P., Brown, C.E., Yang, C., Wang, Z., Zhang, G., Lambert, P., Landriault, M., and Shah, K.: The photolytic behavior of diluted bitumen in simulated seawater by exposed to the natural sunlight. Fuel, 186, 128–139, doi: 10.1016/j.fuel.2016.08.068, 2016.

Yassine, M. M., and Dabek-Zlotorzynska. E.: Application of ultrahigh-performance liquid chromatography–quadrupole time-of-flight mass spectrometry for the characterization of organic aerosol: Searching for naphthenic acids. J. Chromatogr. A, 1512, 22-33, doi: 10.1016/j.chroma.2017.06.067, 2017.

Yue, S., Bikkina, S., Gao, M., Barrie, L. A., Kawamura, K., Fu, P. Sources and radiative absorption of water-soluble brown carbon in the high Arctic atmosphere. Geophys. Res. Letters, 46, 14881–14891. https://doi.org/10.1029/2019GL085318, 2019

Zeng, L., Dibb, J., Scheuer, E., Katich, J. M., Schwarz, J. P., Bourgeois, I., Peischl, J., Ryerson, T., Warneke, C., Perring, A. E., Diskin, G. S., DiGangi, J. P., Nowak, J. B., Moore, R. H., Wiggins, E. B., Pagonis, D., Guo, H., Campuzano-Jost, P., Jimenez, J. L., Xu, L., and Weber, R. J.: Characteristics and evolution of brown carbon in western United States wildfires, Atmos. Chem. Phys., 22, 8009–8036, https://doi.org/10.5194/acp-22-8009-2022, 2022.

Zhang, Y., Shotyk, W., Zaccone, C., Noernberg, T., Pelletier, R., Bicalho, B., Froese, D. G., Davies, L., and Martin J. W.: Airborne Petcoke Dust is a Major Source of Polycyclic Aromatic Hydrocarbons in the Athabasca Oil Sands Region. Environ. Sci. Technol., 50, 4, 1711-1720, doi: 10.1021/acs.est.5b05092, 2016.

Zhou, J., Xiong, C., Pei, X., Kuang, B., Xu, Z., Zhang, F., Song, Y., Li, M., Wang, Z.: Optical properties and cloud condensation nuclei activity of brown carbon containing α–dicarbonyls and reduced nitrogen compounds, Atmos. Res., 293, 106935, doi: 10.1016/j.atmosres.2023.106935, 2023.

Zhu, C. S., Cao, J. J., Huang, R. J., Shen, Z. X.,Wang, Q. Y., and Zhang, N. N.: Light absorption properties of brown carbon over the southeastern Tibetan Plateau. Sci. Total Environ., 625, 246-251, doi: 10.1016/j.scitotenv.2017.12.183, 2018.

Zito, P., Podgorski, D., Johnson, J., Chen, H., Rodgers, R., Guillemette, F., Kellerman, A., Spencer, R., and Tarr, M.: Molecular-Level Composition and Acute Toxicity of Photosolubilized Petrogenic Carbon. Environ. Sci. Technol., 53, 14, 8235-8243, doi: 10.1021/acs.est.9b01894, 2019.